Optimization of BESS Placement and Control Parameters for Frequency Stability in Renewable-Intensive Power Systems

by

Mina Malekan

A thesis submitted to the Faculty of Graduate and Postdoctoral Studies of
The University of Manitoba
in partial fulfillment of the requirements of the degree of

Master of Science

Department of Electrical and Computer Engineering
University of Manitoba
Winnipeg, Canada

Abstract

The increasing integration of renewable energy resources into power systems has heightened the need for advanced optimization methods to maintain the grid's stability and efficiency. This thesis presents a framework that integrates Electromagnetic Transient (EMT) simulations in PSCAD/EMTDC with a genetic algorithm (GA) optimizer, implemented through Python's PyGAD open-source library, to optimize the placement and sizing of battery energy storage systems (BESS). The primary objective is to enhance frequency regulation in response to disturbances caused by the variability of solar power generation. A 12-bus power system, incorporating both synchronous machines and a solar power plant, is modeled and simulated. Candidate BESS locations are selected with the goal of optimization being to determine the most suited location as well as the size of the required BESS. The objective function considers both the frequency nadir and a measure of the cost associated with the number of BESS units deployed. Simulation results show that the GA successfully identifies optimal BESS configurations, demonstrating that without a cost constraint, the optimizer favors the deployment of a large number of units with low droop settings to minimize frequency deviation. Including the cost terms results in a more balanced trade-off between performance and asset cost. The study further highlights the significant impact of BESS placement on system frequency response, underscoring the importance of strategic siting in future grid planning. The proposed EMT-based optimization framework provides a robust and accurate approach for addressing complex, non-linear optimization problems in modern, renewable-rich power systems.

Copyright Notes

Part of the contents of the thesis were included in the following publication presented at the *2025 CIGRE International Symposium*:

- M. Malekan, S. Filizadeh, “Optimization of Battery Energy Storage System Placement and Parameters for Frequency Stability in Renewable-Intensive Power Systems,” in *Proc. CIGRE International Symposium,* Montreal, QC, Oct. 2025.

Acknowledgments

This thesis was made possible through the support and encouragement of many individuals and organizations, to whom I am deeply grateful.

I would like to express my sincere appreciation to my academic advisor, Prof. Shaahin Filizadeh, for his continuous guidance, insightful feedback, and steadfast encouragement throughout the course of this research.

I gratefully acknowledge the University of Manitoba and the Natural Sciences and Engineering Research Council of Canada (NSERC) for their financial support, which enabled the completion of this work.

I am profoundly thankful to my husband, Ramin, for his unwavering support, patience, and understanding throughout this journey.

Lastly, I extend my gratitude to my family, colleagues at the University of Manitoba, and friends for their constant support and encouragement in countless ways during my research.

To Ramin

Table of Contents

List of Tables

List of Figures

List of Acronyms

AVM	Average-value model
BESS	Battery energy storage system
EMT	Electromagnetic transient(s)
GA	Genetic algorithm
IBR	Inverter-based resource(s)
OE-EMTS	Optimization-enabled electromagnetic transient simulation
OF	Objective function
RES	Renewable energy sources
VSC	Voltage source converter

Chapter 1

Introduction

1.1 Background and Literature Review

1.1.1 Diminishing Inertia in Power Systems

The growing penetration of renewable energy sources (RES) has changed the generation portfolio of modern power systems. This transition is primarily driven by escalating environmental concerns — particularly the urgent need to reduce greenhouse gas emissions — and by the escalating depletion of conventional fossil fuel reserves [1]. In addition, the rapid decline in the capital costs of photovoltaic (PV) and wind power generation technologies has further accelerated this transition. Faster installation and commissioning processes, modular system designs, and strong government incentives with supportive energy policies have also played key roles [2,3]. Together, these factors have significantly reduced the barriers to RES deployment, allowing for large-scale expansion and smooth integration into existing power grids.

System inertia reflects a power system's ability to resist rapid frequency changes during supply-demand imbalances. The system frequency serves as an indicator of the degree of imbalance between power supply and demand. Traditionally, synchronous machines with heavy rotating masses provide this inertia by absorbing or releasing kinetic energy, helping to maintain stability and limit frequency excursions. However, the growing replacement of conventional generators with converter-based renewable sources significantly reduces inertia, weakening the response of frequency and increasing instability risks. As a result, frequency regulation has become a critical challenge in modern power systems with diminishing inertia. Significant concerns arise from large frequency deviations, including damage to generating units, potential equipment malfunction, and transmission line overloading, all of which can create unstable conditions that pose serious challenges to power system reliability and operation [4–6]. A typical frequency response in a power system following a supply–demand imbalance is illustrated in Figure 1.1 [7].

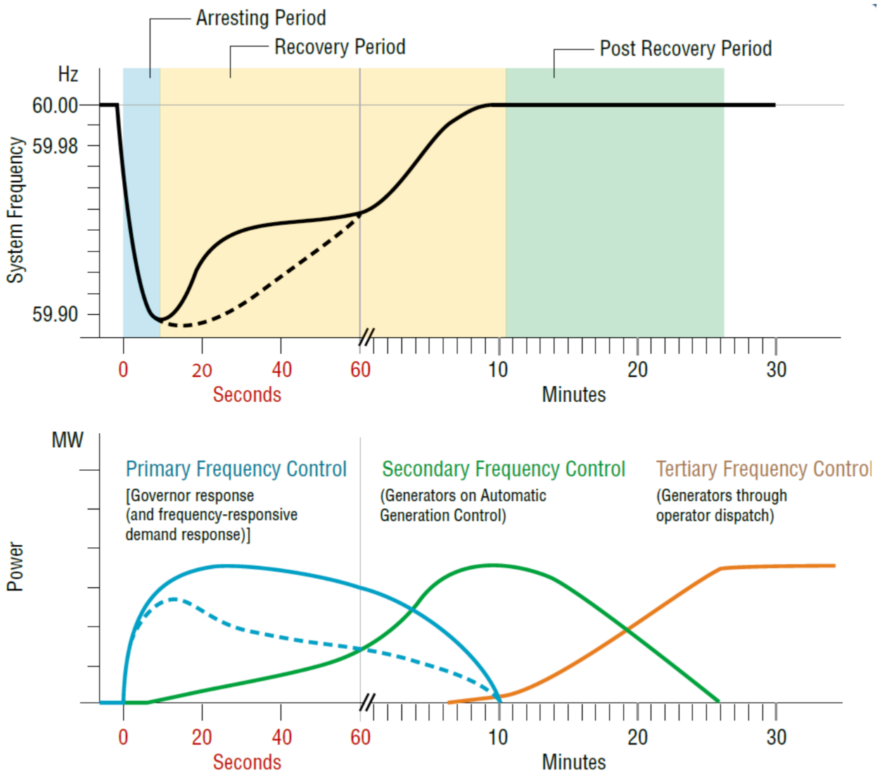

Figure 1.1: Typical response of frequency in a power system [7].

Ignoring the governor action, the initial stage of this response, known as the *inertial response*, can be represented by the swing equation given as follows [8]:

$$2H\frac{\mathrm{d}f}{\mathrm{d}t} = P_{\mathrm{gen}} - P_{\mathrm{load}} \tag{1.1}$$

where H is the system inertia in seconds, f is system frequency in pu, P_{gen} is the generated power in pu, and P_{load} is the load demand in pu. The inertial response is commonly characterized by two parameters: the rate of change of frequency ($RoCoF$) and the frequency nadir (f_{nadir}); $RoCoF$ represents the initial slope of the inertial response following a supply–demand imbalance, and f_{nadir} denotes the lowest frequency reached during the event. Based on the swing equation and the shape of the inertial response, both parameters are inversely proportional to the system inertia (H). Consequently, reduced inertia worsens frequency stability and may lead to violations of frequency regulation standards established by transmission system operators (TSOs). For instance the European Network of Transmission System Operators for Electricity (ENTSO-E) requires generating units to withstand $RoCoF$ up to ± 2.0 Hz/s for 0.5 seconds, ± 1.5 Hz/s for 1 second, and ± 1.25 Hz/s for 2 seconds without disconnecting from the grid [9]. Also, the frequency must remain above 49.0 Hz for normal contingencies (e.g., generator trip) and above 47.5 Hz for extreme disturbances (system splits or severe imbalances) [10].

1.1.2 Solutions to Low-Inertia Systems

Various solutions have been proposed in the literature to address the challenges posed by low-inertia power systems. One practical approach is the direct augmentation of rotating masses through synchronous condensers (SCs), which store kinetic energy in their rotors and release or absorb energy during power imbalances [11]. However, the considerable operating and capital costs associated with synchronous condensers have limited their widespread adoption for improving system inertia [12]. Converter-interfaced energy storage devices have also been investigated in the literature. DC-link capacitors, which are primarily used to maintain the DC-side voltage of voltage source converters (VSCs), are utilized to support the system in frequency events. While tolerating a dip in the DC voltage, the energy stored in these capacitors is tapped into to assist the system undergoing frequency deviations [13–15]. These small amounts of energy, however, are typically insufficient for use during major frequency events. Superconducting magnetic energy storage systems (SMESSs) utilize direct current and store energy within a magnetic field; they have been proposed for regulation of frequency in [16, 17]. To deliver fast frequency support, [18] incorporated supercapacitors in a hybrid power plant. An accurate dynamic model of supercapacitor banks is presented for power system simulations in [19] highlighting their high power density and rapid response, thus making them promising for fast frequency support and transient stability enhancement.

Among all energy storage devices, battery energy storage systems (BESSs) have been at the center of attention for several reasons. As shown in Figure 1.2, lithium-ion battery pack prices have continued their long-term downward trend, reaching a record low global average of US$108/kWh in 2025—an 8% decline from the previous year and a remarkable 93% reduction since 2010 [20]. BESS offers near-instantaneous response times (milliseconds to seconds), ideal for ancillary services such as frequency control and black-start capabilities [21–25]. Lithium-ion BESS have also been reported to achieve 90%+ round-trip efficiency, high energy density, and long cycle life (thousands of cycles) [26–28].

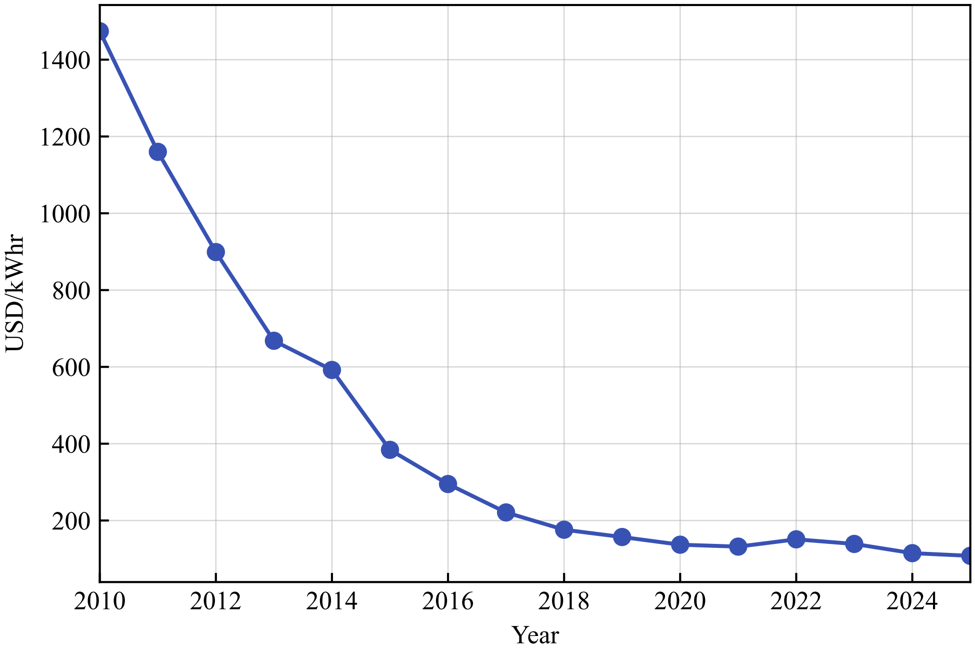

Figure 1.2: Downward trend of battery pack prices; adopted from [29].

1.1.3 Challenges in Modeling and Simulation of BESS in Power Systems

Computer simulation models play vital rules in studying BESS connected to power systems. The model must accurately and efficiently (from a computational viewpoint) exhibit the dynamics of the BESS under various conditions such as de-blocked and blocked modes. However, for certain studies—for instance, when the BESS is assumed to operate in the de-blocked mode throughout the entire simulation time—the blocked mode may not be included.

A typical BESS consists of a battery, a DC-DC converter, and a 2-level VSC. Modeling BESS for power system studies involves capturing the dynamics of batteries, converters, and controls across various timescales including slow dynamics of the battery's electrochemical process and fast and nonlinear dynamics of the units associated with the converter's control. Such dynamics necessitate the use of Electromagnetic Transient (EMT) simulation to accurately capture detailed interactions between power electronic devices and the grid, ensuring reliable operation and planning [30].

Modeling each switching element as a separate component allows for a highly accurate representation of switching details. However, this approach suffers from the drawback of long simulation times, as the conductance matrix of the entire network model must be re-inverted each time a switch changes state. The situation becomes even more challenging when multiple BESS units are connected to the grid at different bus locations for optimization purposes.

To address this, average-value models (AVMs) are employed to approximate the system's behavior by averaging the quantities of interest over successive switching cycle. AVMs preserve the low-frequency dynamics relevant to grid interactions while eliminating high-frequency ripples [31, 32] caused by switching. Such models maintain a constant conductance matrix, thereby reducing the computational demands of the simulations.

1.1.4 Optimization of BESS Placement for Frequency Regulation

Rapid integration of renewable energy resources into power systems has escalated the need for advanced optimization techniques to ensure grid stability and efficiency. BESS are pivotal in addressing the intermittency of renewable resources such as solar PV and wind power, providing critical services such as frequency regulation, voltage support, and energy arbitrage. However, determining the optimal placement and sizing of BESS within a power network is a complex, nonlinear problem that requires sophisticated computational approaches. This thesis proposes a framework that combines EMT simulations with genetic algorithms (GA) to optimize BESS placement, enhancing power system performance under high renewable penetration.

Numerous studies have explored optimal BESS placement, targeting various objectives. For instance, the authors of [33] developed a two-stage framework using the Harris Hawks Optimization algorithm to boost microgrid self-consumption and hosting capacity under high renewable penetration, achieving reduced power losses through strategic BESS placement. The work in [34] introduced a DC optimal power flow-based approach for simultaneous BESS sizing and placement, enhancing system reliability in a 24-bus IEEE test system. By solving a multi-objective problem, [35] tackled BESS sizing and allocation for voltage regulation, factoring in battery lifespan and employing an elitist non-dominated sorting GA to minimize energy losses and enhance voltage profiles. Additionally, [36] proposed a stochastic planning framework for BESS in distribution networks with significant wind power, utilizing Monte Carlo simulation and differential evolution to optimize wind power usage while reducing costs. Most of these studies were conducted on non-EMT platforms. However, the growing presence of inverter-based resources (IBRs) underscores the need for EMT simulations to ensure accuracy. The integration of EMT simulations with optimization techniques has led to optimization-enabled EMT simulation (OE-EMTS), previously applied in tasks such as tuning the parameters of converter-intensive power systems [37], designing controllers for HVDC systems [38], and optimizing parameters of a grid-forming modular multilevel converter [39].

Among various optimization techniques, this thesis adopts the GA for the following reasons:

- The problem addressed is inherently non-linear, involving both continuous and discrete parameters, with a complex objective function (OF) that may not be explicitly expressed in a mathematical formulation.
- The main benefit of GA is that it does not rely on gradient information, making it well-suited for finding the global optimum while avoiding local optima [40].

This thesis aims at integrating EMT simulations with the flexibility of GA, facilitated by the open-source PyGAD library [41] in Python. By utilizing simulation automation processes [42], the proposed methodology facilitates seamless interaction between GA and EMT simulations, optimizing BESS placement to improve frequency regulation. The approach optimizes parameters such as BESS location, number of BESS units, and droop gains, employing a fitness function derived from EMT simulation outputs to achieve an optimal OF value. The OF combines the frequency nadir, which is a measure of the system's operating fitness, with BESS cost, which is a measure of deployment feasibility, thus balancing competing objectives.

1.2 Motivation

This thesis is motivated by the need to identify optimal location(s) within a power grid for integrating BESS to enhance the system frequency response. It is worth noting that BESS can also improve voltage stability; however, this study specifically focuses on improving frequency stability. In addition to technical considerations, the optimization process indirectly accounts for the cost implications associated with BESS deployment. While existing research provides a strong foundation, several gaps remain that this work aims to address.

Current approaches to BESS placement optimization often rely on phasor-domain models, which overlook EMT details that are critical during fast dynamics. This limitation is significant because BESS control systems typically operate at much faster timescales than electromechanical transients. Furthermore, detailed EMT models of BESS—arising from switching device representations—are computationally intensive, leading to prohibitively long simulation times. To overcome this challenge, this thesis develops average-value models that preserve dynamic accuracy while reducing simulation runtime in EMT platforms.

Another gap identified in the literature is the absence of automated frameworks integrating EMT programs with external optimization engines. Such frameworks are crucial for leveraging EMT simulators as objective function evaluators while utilizing advanced optimization algorithms—such as those implemented in Python—to optimize power system objectives efficiently.

1.3 Outline of the Thesis

The remainder of this thesis is structured as follows.

> **Chapter 2:** This chapter develops the average-value model of the BESS, encompassing the battery, DC-DC converter, and 2-level VSC using circuit averaging techniques. It also examines the control strategies for both the DC-DC converter and the VSC, designed to regulate active and reactive power injection at the point of interconnection.
>
> **Chapter 3:** A conceptual and methodological framework is introduced for integrating EMT simulations in PSCAD/EMTDC with Python-based optimization workflows. The goal is to create an automated, iterative process that performs parameter tuning, simulation execution, performance evaluation through objective functions, and convergence using optimization algorithms—eliminating manual intervention. This framework is particularly applicable to power system design and control tasks where transient dynamics are critical, such as controller tuning, fault response optimization, and stability improvement.
>
> **Chapter 4:** This chapter investigates the optimal placement of BESS within a 12-bus benchmark power system using OE-EMTS with a GA optimizer. The system includes synchronous generators and a solar power plant. Candidate locations for BESS are evaluated to determine

both the most suitable placement and the required size. The objective function considers frequency nadir and the cost implications of BESS units.

Chapter 5: This chapter concludes the thesis with a summary of its contributions, conclusions made, and recommendations for future research.

Chapter 2

Modeling and Control of BESS

The overall structure of a BESS is illustrated in Figure 2.1, which includes a battery pack, a DC-DC converter, and a VSC [43, 44]. The DC-DC converter boosts the battery voltage to a desired level for use by the VSC. The DC-link capacitor maintains the DC voltage, providing a relatively constant voltage for the VSC to convert into three-phase AC voltages, thereby delivering active and reactive power to the grid. In this thesis, multiple BESSs are connected to the grid at different bus locations for optimization purposes. However, only one BESS is active during each simulation, while the others remain in idle mode.

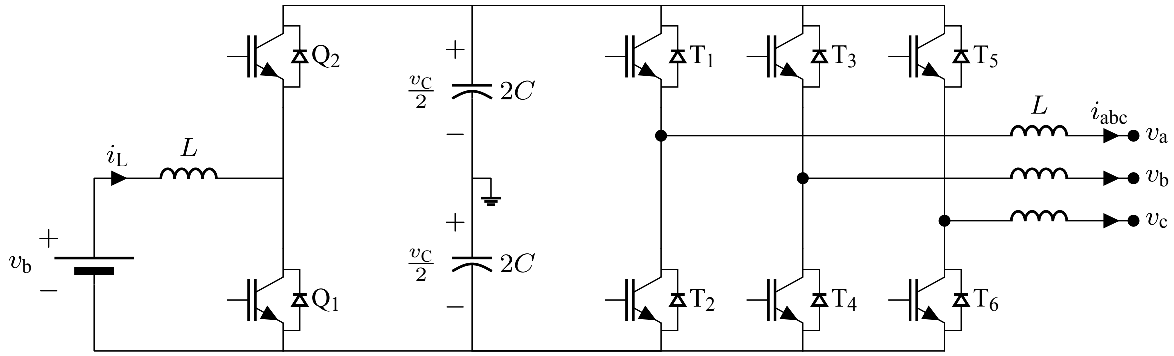

Figure 2.1: Schematic diagram of a battery energy storage system.

This approach avoids lengthy, repetitive initialization periods required for synchronous machines in the grid, during which all BESSs operate in idle mode. When a contingency occurs, the selected BESS at a specific bus is commanded to inject power into the grid to stabilize frequency. Although most BESSs are in idle mode, they remain connected to the network and are included in the network solution. Employing detailed switching models for these BESSs would be computationally intensive, as the conductance matrix of the entire network must be updated and re-inverted at every time step. To mitigate this issue, an average-value model (AVM) for the BESS is developed in the following sections. This model simplifies the detailed circuit by eliminating switching dynamics while preserving the low-frequency behavior of the converter, which aligns with the scope of the thesis—focusing on the BESS behavior from the grid's perspective, where internal switching events are of lesser concern.

2.1 Modeling of a Battery

Various battery models, such as electrochemical and circuit-based models, have been explored in the literature. Electrochemical models involve solving partial differential equations to describe ion and electron movements during chemical reactions. However, the level of detail provided by these models is often unnecessary for power system applications. In contrast, circuit-based models represent the battery's terminal voltage-current relationship. The simplest circuit-based model consists of an internal voltage source in series with its internal resistance. In practice, the battery's internal voltage decreases as it charges/discharges. To account for this, the Shepherd equation calculates the internal voltage based on the battery's state-of-charge (SOC) [45]. This model is illustrated in Figure 2.2.

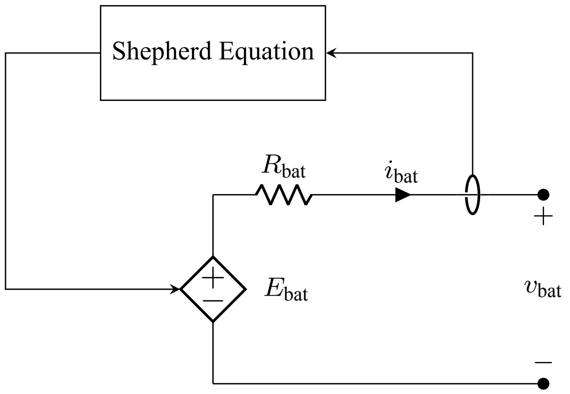

Figure 2.2: Equivalent circuit a battery according to Shepherd's model.

The Shepherd equation is given by [45]

$$E_{\text{bat}} = E_0 - \frac{K}{SOC} + A\mathrm{e}^{-BQ_{\text{full}}\left(1-SOC\right)}, \tag{2.1}$$

where

$$A = E_{\text{full}} - E_{\text{exp}} \tag{2.2}$$

$$B = \frac{3}{Q_{\text{exp}}} \tag{2.3}$$

$$K = \Big(E_{\text{full}} - E_{\text{nom}} + A(\mathrm{e}^{-BQ_{\text{nom}}} - 1)\Big) \times \frac{Q_{\text{full}} - Q_{\text{nom}}}{Q_{\text{nom}}} \tag{2.4}$$

$$E_0 = E_{\text{full}} + K - A \tag{2.5}$$

and

E_{bat} is the battery's no-load voltage [V],

SOC is the state-of-charge [pu],

E_{full} is the voltage when the battery is full [V],

Q_{full} is the battery capacity [Ah],

E_{exp} is the exponential voltage [V],

Q_{exp} is the exponential capacity [Ah],

E_{nom} is the nominal voltage [V], and

Q_{nom} is the nominal capacity [Ah].

The SOC can be calculated using the initial SOC (SOC_{init}), battery current, and full battery capacity as follows:

$$SOC = SOC_{\text{init}} - \frac{\int_0^t i_{\text{bat}}(\tau)\ \mathrm{d}\tau}{Q_{\text{full}}} = SOC_{\text{init}} - \frac{Q}{Q_{\text{full}}}, \tag{2.6}$$

where Q denotes the accumulated discharged/charged capacity over the time interval $[0, t]$. The parameters of a typical battery unit are given in Table 2.1. Note that the per-unit values are expressed using E_{nom} as the voltage base and Q_{full} as the capacity base. Using these parameters, the discharge curve— i.e., the battery's internal voltage as a function of its accumulated discharged capacity—is plotted in Figure 2.3, with the corresponding parameters indicated.

Table 2.1: Parameters of a typical battery unit.

Parameter	E_{nom}	Q_{full}	E_{full}	E_{exp}	Q_{nom}	Q_{exp}
Value	0.5	0.0167	1.15	1.03	0.95	0.4
Unit	kV	kAhr	pu	pu	pu	pu

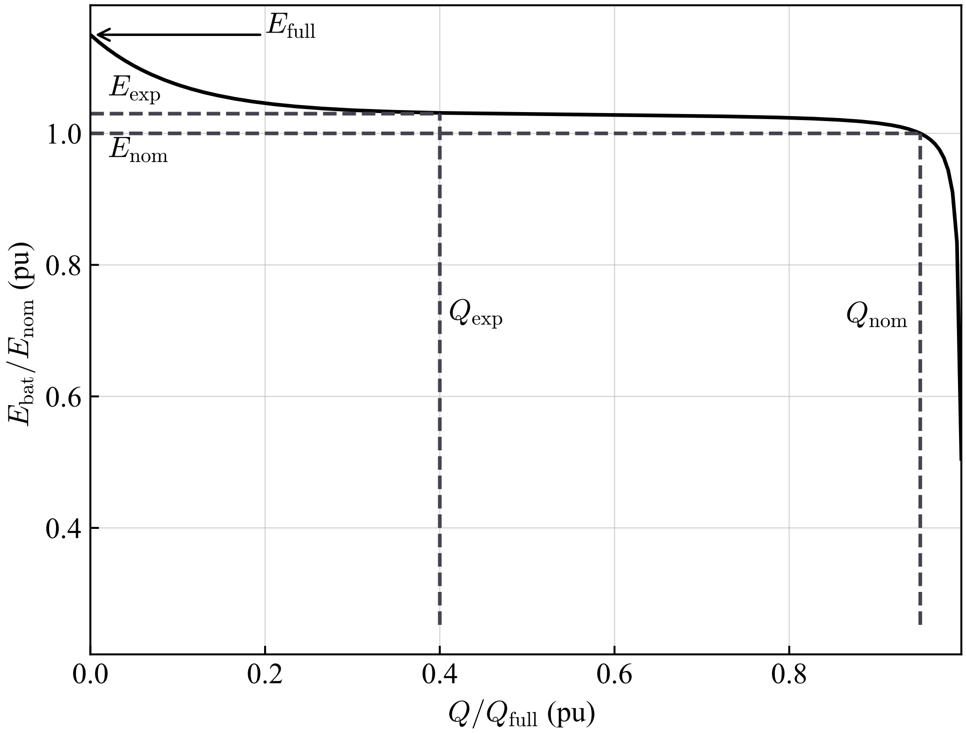

Figure 2.3: A typical battery discharge curve.

2.2 Principles of Average-Value Modeling

Average-value models are commonly used to represent power electronic systems, particularly those involving high-frequency switching events. Unlike detailed switching models that capture individual switching actions, averaged-value models neglect the rapid switching effects within each cycle and instead consider the system's low-frequency behavior.

To determine the average-value model of a switching power electronic converter with a switching period T_s, the average value of a signal $x(t)$ over one switching period is defined as

$$\langle x(t)\rangle_{T_\mathrm{s}} = \frac{1}{T_\mathrm{s}} \int_{t-T_\mathrm{s}}^{t} x(\tau)\ \mathrm{d}\tau. \tag{2.7}$$

This averaging operation filters out the high-frequency switching components of the signal, capturing its low-frequency contents. In the AVM for power electronic converters, continuous (and often slowly varying) waveforms, such as capacitor voltages and inductor currents, are typically assumed constant within a single switching period, although they may vary across periods. In other words, it is assumed that the electrical time-constants of the converter are much longer than the switching period, T_s. Under this assumption, the average of the switched signal $s(t)x(t)$, where $s(t)$ is a switching function taking values of 0 or ± 1, is derived as follows:

$$\langle s(t)x(t)\rangle_{T_\mathrm{s}} = \frac{1}{T_\mathrm{s}} \int_{t-T_\mathrm{s}}^{t} s(\tau)x(\tau)\ \mathrm{d}\tau = \langle x(t)\rangle_{T_\mathrm{s}} \times \frac{1}{T_\mathrm{s}} \int_{t-T_\mathrm{s}}^{t} s(\tau)\ \mathrm{d}\tau = \langle x(t)\rangle_{T_\mathrm{s}} \times \langle s(t)\rangle_{T_\mathrm{s}} \tag{2.8}$$

Notably, $\langle s(t)\rangle_{T_\mathrm{s}}$ represents the duty cycle of the switching signal $s(t)$.

2.3 Average-Value Model of the DC-DC Converter

A bidirectional DC-DC converter is depicted in Figure 2.4, with the switching network highlighted. The circuit averaging method, as described in [46], is applied to derive the average-value model of the converter. The key step in circuit averaging involves replacing the switching network with averaged dependent voltage and current sources.

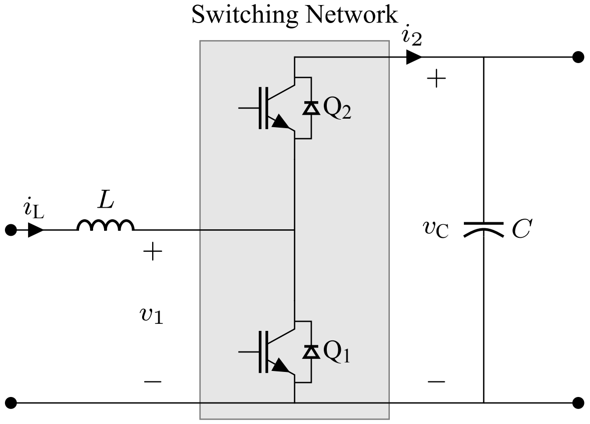

Figure 2.4: Bidirectional DC-DC converter.

The first step is to establish relationships among the terminal quantities, namely terminal voltages and currents. Switched waveforms are expressed in terms of continuous state variables and switching functions. In this DC-DC converter, the voltage v_1 and current i_2 are the switched waveforms, while the other terminal quantities, i_L and v_C, are continuous (and slowly varying) state variables. The relationships between these variables are given by:

$$v_1(t) = (1 - q(t))v_C(t) \tag{2.9}$$

$$i_2(t) = (1 - q(t))i_L(t) \tag{2.10}$$

where $q(t)$ is the switching function defined as

$$q(t) = \begin{cases} 1 & Q_1\text{: on, } Q_2\text{: off} \\ 0 & Q_1\text{: off, } Q_2\text{: on} \end{cases} \tag{2.11}$$

The second step involves applying the averaging operator to these equations, yielding:

$$\langle v_1(t)\rangle_{T_s} = (1 - \langle q(t)\rangle_{T_s}) \times \langle v_C(t)\rangle_{T_s} = (1 - d(t)) \times \langle v_C(t)\rangle_{T_s} \tag{2.12}$$

and

$$\langle i_2(t)\rangle_{T_s} = (1 - \langle q(t)\rangle_{T_s}) \times \langle i_L(t)\rangle_{T_s} = (1 - d(t)) \times \langle i_L(t)\rangle_{T_s} \tag{2.13}$$

where $d(t)$ is the duty cycle of the converter. The final step is to convert the averaged equations into a circuit model using dependent voltage and current sources, as shown in Figure 2.5. Here, the switching network is replaced with the averaged model.

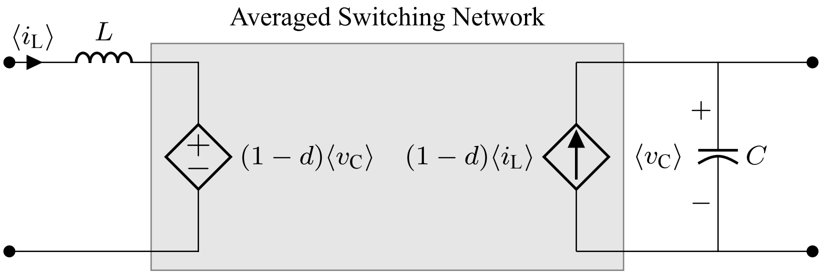

Figure 2.5: Average-value model of the DC-DC converter.

2.4 Average-Value Model of the VSC

Figure 2.6 illustrates a 2-level VSC with its DC side split into two capacitors with their midpoint grounded. This ground serves as the reference for the terminal voltages v_{ta}, v_{tb}, and v_{tc}.

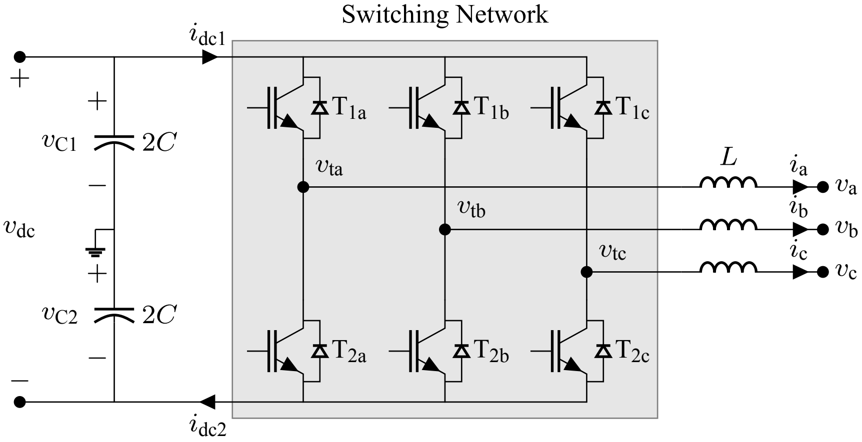

Figure 2.6: Circuit diagram of the VSC.

Applying Kirchhoff's current law (KCL) to the cut-set involving currents i_{a}, i_{b}, i_{c}, i_{dc1}, and i_{dc2}, the following expression is derived.

$$i_{\mathrm{dc1}} - i_{\mathrm{dc2}} = i_{\mathrm{a}} + i_{\mathrm{b}} + i_{\mathrm{c}} \tag{2.14}$$

Assuming balanced three-phase AC currents, the DC currents i_{dc1} and i_{dc2} are equal:

$$i_{\mathrm{dc1}} = i_{\mathrm{dc2}} = i_{\mathrm{dc}} \tag{2.15}$$

The DC terminal current entering the positive rail exits at the negative rail, resulting in identical currents through the upper and lower capacitors on the DC bus. Thus, the capacitor voltages are equal, each being half of the total DC link voltage

$$v_{\mathrm{C1}} = v_{\mathrm{C2}} = \frac{v_{\mathrm{dc}}}{2} \tag{2.16}$$

To derive the AVM of the VSC, the switching functions for the three phases are defined as follows.

$$s_j(t) = \begin{cases} 1 & \mathrm{T}_{1j}\text{: on, } \mathrm{T}_{2j}\text{: off} \\ \\ -1 & \mathrm{T}_{1j}\text{: off, } \mathrm{T}_{2j}\text{: on} \end{cases} \quad ; \qquad j \in \{\text{a, b, c}\} \tag{2.17}$$

The converter's terminal voltages correspond to either the positive or negative DC-rail voltage and can be expressed using the DC voltage and the respective switching function (i.e., s_{a}, s_{b}, ors_{c}) as follows:

$$\begin{aligned} v_{\mathrm{ta}} &= s_{\mathrm{a}} \frac{v_{\mathrm{dc}}}{2} \\ v_{\mathrm{tb}} &= s_{\mathrm{a}} \frac{v_{\mathrm{dc}}}{2} \\ v_{\mathrm{tc}} &= s_{\mathrm{a}} \frac{v_{\mathrm{dc}}}{2} \end{aligned} \tag{2.18}$$

Similarly, the DC current is the sum of the AC currents switched by either the upper or lower switches, expressed as follows.

$$i_{\mathrm{dc}} = \frac{s_{\mathrm{a}}+1}{2} i_{\mathrm{a}} + \frac{s_{\mathrm{b}}+1}{2} i_{\mathrm{b}} + \frac{s_{\mathrm{c}}+1}{2} i_{\mathrm{c}} \tag{2.19}$$

which is further simplified into the following equation considering balanced three phase currents.

$$i_{\mathrm{dc}} = \frac{s_{\mathrm{a}}}{2} i_{\mathrm{a}} + \frac{s_{\mathrm{b}}}{2} i_{\mathrm{b}} + \frac{s_{\mathrm{c}}}{2} i_{\mathrm{c}} \tag{2.20}$$

Applying the averaging operator to these equations yields the following averaged equations

$$\begin{aligned}\langle v_{\mathrm{ta}}\rangle_{T_{\mathrm{s}}} &= m_{\mathrm{a}}\frac{\langle v_{\mathrm{dc}}\rangle_{T_{\mathrm{s}}}}{2}\\ \langle v_{\mathrm{tb}}\rangle_{T_{\mathrm{s}}} &= m_{\mathrm{b}}\frac{\langle v_{\mathrm{dc}}\rangle_{T_{\mathrm{s}}}}{2}\\ \langle v_{\mathrm{tc}}\rangle_{T_{\mathrm{s}}} &= m_{\mathrm{c}}\frac{\langle v_{\mathrm{dc}}\rangle_{T_{\mathrm{s}}}}{2}\end{aligned} \tag{2.21}$$

$$\langle i_{\mathrm{dc}}\rangle_{T_{\mathrm{s}}} = \frac{m_{\mathrm{a}}\langle i_{\mathrm{a}}\rangle_{T_{\mathrm{s}}} + m_{\mathrm{b}}\langle i_{\mathrm{b}}\rangle_{T_{\mathrm{s}}} + m_{\mathrm{c}}\langle i_{\mathrm{c}}\rangle_{T_{\mathrm{s}}}}{2} \tag{2.22}$$

where m_{a}, m_{b}, and m_{c}, known as modulation waveforms, represent the average values of the switching functions s_{a}, s_{b}, and s_{c}, respectively. These averaged equations are converted into a circuit model, as shown in Figure 2.7, representing the AVM of the VSC, where the switching network is replaced with averaged voltage and current sources. Note that the averaging symbol, $\langle . \rangle$, will be omitted in the subsequent equations for notational brevity.

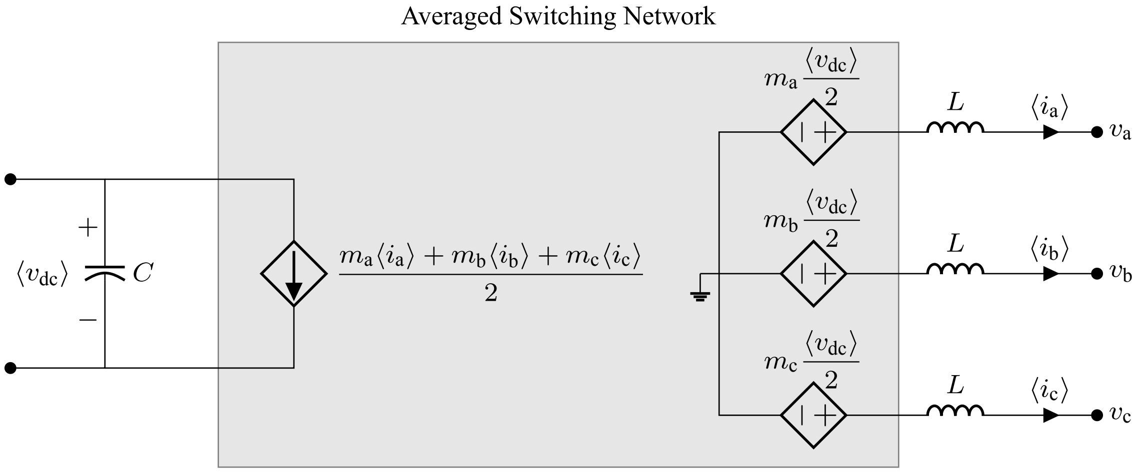

Figure 2.7: Average-value model of the VSC.

2.5 BESS Control

The control of a BESS, comprising a battery, bidirectional DC-DC converter, and VSC, can be configured in multiple ways depending on which variables are prioritized [47]. There are three key control variables, namely the DC-link voltage, active power, reactive power (or alternatively, AC voltage magnitude). The reactive power (or AC voltage) is always controlled solely by the VSC. In contrast, the DC-link voltage and active power can be assigned either to the DC-DC converter or the VSC, leading to two complementary control modes.

In the first mode, the DC-DC converter regulates DC link voltage via its duty cycle while the VSC controls active power. In the second mode, however, the DC-DC converter regulates active power, which is nearly identical to the battery DC power, by controlling inductor/battery current via its duty cycle while the VSC maintains DC voltage.

In this thesis, the first mode is adopted for BESS control. Additionally, reactive power (rather than AC voltage magnitude) is selected as the control variable. These control strategies are detailed in the following subsections.

2.5.1 Control of the DC-DC Converter

A block diagram of the DC-DC converter control is shown in Figure 2.8. The DC-link voltage is measured and compared with the reference value to generate an error signal, which is then fed to a proportional-integral (PI) controller. The controller outputs the duty cycle of the converter, driving the error to zero.

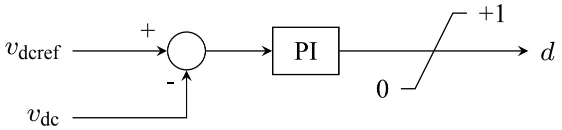

Figure 2.8: Feedback control system of the DC-DC converter.

2.5.2 Control of the Voltage Source Converter

VSCs are typically controlled in a synchronously-rotating dq frame, where AC sinusoidal signals are transformed into DC quantities under steady-state conditions [48]. This enables the use of simple PI controllers to eliminate steady-state errors. The dq0 transformation adopted in this thesis is realized through the following matrix equation [48]:

$$\begin{bmatrix} f_{\text{d}} \\ f_{\text{q}} \\ f_0 \end{bmatrix} = \frac{2}{3} \begin{bmatrix} \cos(\theta) & \cos(\theta - 120^\circ) & \cos(\theta + 120^\circ) \\ \sin(\theta) & \sin(\theta - 120^\circ) & \sin(\theta + 120^\circ) \\ 1 & 1 & 1 \end{bmatrix} \begin{bmatrix} f_{\text{a}} \\ f_{\text{b}} \\ f_{\text{c}} \end{bmatrix} \tag{2.23}$$

where the three-phase signals f_{a}, f_{b}, f_{c} are transformed into f_{d}, f_{q}, f_0 using the transformation angle θ. In this thesis, all three-phase signals are assumed balanced, resulting in a zero-axis quantity $f_0 = 0$. The inverse transformation is as follows.

$$\begin{bmatrix} f_{\text{a}} \\ f_{\text{b}} \\ f_{\text{c}} \end{bmatrix} = \begin{bmatrix} \cos(\theta) & \sin(\theta) & 1 \\ \cos(\theta - 120^\circ) & \sin(\theta - 120^\circ) & 1 \\ \cos(\theta + 120^\circ) & \sin(\theta + 120^\circ) & 1 \end{bmatrix} \begin{bmatrix} f_{\text{d}} \\ f_{\text{q}} \\ f_0 \end{bmatrix} \tag{2.24}$$

While the transformation angle θ can be chosen arbitrarily, it is typically selected such that $\omega = \frac{\text{d}\theta}{\text{d}t}$; while ω may be arbitrarily assigned, it is often selected to be the network's angular frequency.

This choice yields a synchronously rotating reference frame in which three-phase quantities appear as DC signals under steady-state conditions. To illustrate this, consider a three-phase sinusoidal waveform with a constant angular frequency ω_0. Let the transformation angle be $\theta = \omega_0 t + \theta_0$, where θ_0 is a constant initial angle. The transformed signals are then obtained as follows

$$\begin{bmatrix} v_\mathrm{a} \\ v_\mathrm{b} \\ v_\mathrm{c} \end{bmatrix} = \begin{bmatrix} V_\mathrm{m}\cos(\omega_0 t) \\ V_\mathrm{m}\cos(\omega_0 t - 120^\circ) \\ V_\mathrm{m}\cos(\omega_0 t + 120^\circ) \end{bmatrix} \xrightarrow{\theta=\omega_0 t+\theta_0} \begin{bmatrix} v_\mathrm{d} \\ v_\mathrm{q} \\ v_0 \end{bmatrix} = \begin{bmatrix} V_\mathrm{m}\cos(\theta_0) \\ -V_\mathrm{m}\sin(\theta_0) \\ 0 \end{bmatrix} \tag{2.25}$$

showing that the dq0 components become DC signals. It is important to highlight that the q-component becomes zero when $\theta_0 = 0$, i.e., when the the transformation angle is aligned with the phase angle of the phase-a voltage at the point of common coupling (PCC). During transients, however, the angular frequency is no longer constant and may vary with time, causing the dq components to vary as well.

The instantaneous active and reactive power in the dq0 frame are expressed as [48]

$$\begin{aligned} P &= \frac{3}{2}\left(v_\mathrm{d} i_\mathrm{d} + v_\mathrm{q} i_\mathrm{q}\right) \\ Q &= \frac{3}{2}\left(v_\mathrm{d} i_\mathrm{q} - v_\mathrm{q} i_\mathrm{d}\right). \end{aligned} \tag{2.26}$$

By aligning the transformation angle with the PCC voltage, the power equations simplify to

$$\begin{aligned} P &= \frac{3}{2} v_\mathrm{d} i_\mathrm{d} = \frac{3}{2} V_\mathrm{m} i_\mathrm{d} \\ Q &= \frac{3}{2} v_\mathrm{d} i_\mathrm{q} = \frac{3}{2} V_\mathrm{m} i_\mathrm{q} \end{aligned} \tag{2.27}$$

showing that the active and and reactive power are separately controlled with the direct and quadrature current components, respectively.

To derive the block diagram representation of the VSC in the dq reference frame, the Kirchhoff's voltage law (KVL) equations at the VSC terminals can be expressed as follows:

$$\begin{aligned} L\frac{\mathrm{d}i_{\mathrm{a}}}{\mathrm{d}t} + Ri_{\mathrm{a}} &= m_{\mathrm{a}}\frac{v_{\mathrm{dc}}}{2} - v_{\mathrm{a}} \\ L\frac{\mathrm{d}i_{\mathrm{b}}}{\mathrm{d}t} + Ri_{\mathrm{b}} &= m_{\mathrm{b}}\frac{v_{\mathrm{dc}}}{2} - v_{\mathrm{b}} \\ L\frac{\mathrm{d}i_{\mathrm{c}}}{\mathrm{d}t} + Ri_{\mathrm{c}} &= m_{\mathrm{c}}\frac{v_{\mathrm{dc}}}{2} - v_{\mathrm{c}} \end{aligned} \tag{2.28}$$

where L and R represent the per-phase inductance and resistance of the interface transformer connecting the VSC to the PCC. Transforming these equations into the dq reference frame yields:

$$\begin{aligned} L\frac{\mathrm{d}i_{\mathrm{d}}}{\mathrm{d}t} + Ri_{\mathrm{d}} &= m_{\mathrm{d}}\frac{v_{\mathrm{dc}}}{2} - v_{\mathrm{d}} - \omega L i_{\mathrm{q}} \\ L\frac{\mathrm{d}i_{\mathrm{q}}}{\mathrm{d}t} + Ri_{\mathrm{q}} &= m_{\mathrm{q}}\frac{v_{\mathrm{dc}}}{2} - v_{\mathrm{q}} + \omega L i_{\mathrm{d}} \end{aligned} \tag{2.29}$$

which may then be represented in the block diagram shown in Figure 2.9. Note that m_{d} and m_{q} are the dq components of the modulation waveforms m_{a}, m_{b}, and m_{c}.

As shown in Figure 2.9 the d- and q-axis currents are coupled, preventing their independent control via m_{d} and m_{q}, respectively. To address this issue, the decoupled control strategy, as depicted in Figure 2.10, is employed to mitigate the effect of coupling [49]. Additionally, the model includes nonlinear multiplication by $\frac{v_{\mathrm{dc}}}{2}$, which is compensated in the control block diagram by an equivalent division by $\frac{v_{\mathrm{dc}}}{2}$. Note that the reference currents i_{dref} and i_{qref} can be calculated from the reference active and reactive powers described by

$$i_{\mathrm{dref}} = \frac{P_{\mathrm{ref}}}{\frac{3}{2}V_{\mathrm{m}}} \qquad , \qquad i_{\mathrm{qref}} = \frac{Q_{\mathrm{ref}}}{\frac{3}{2}V_{\mathrm{m}}}. \tag{2.30}$$

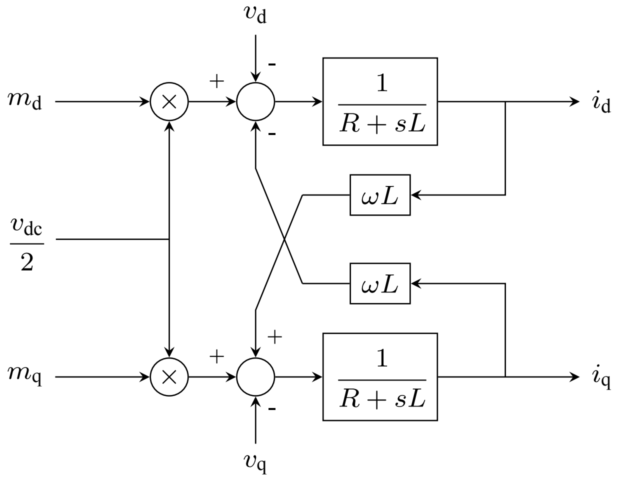

Figure 2.9: Functional block diagram of a VSC connected to the PCC via a transformer.

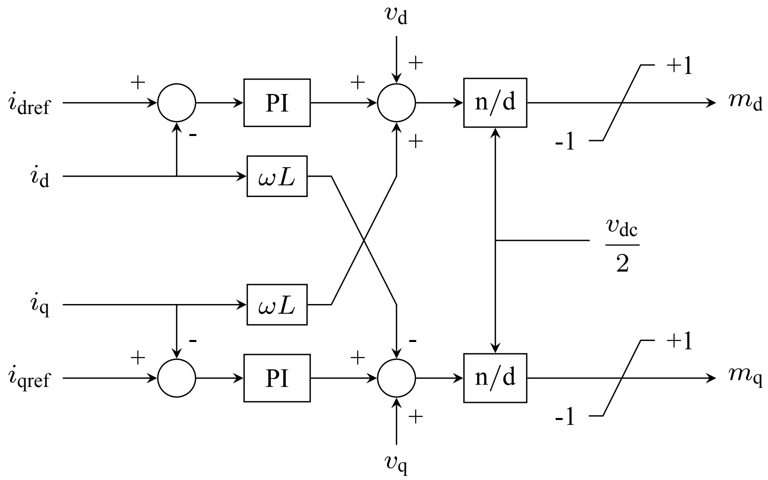

Figure 2.10: Feedback control system of the VSC with decoupled control strategy.

2.6 Validation of the DC-DC Converter Model

To validate the AVM against a detailed switching model, a controlled DC–DC converter (Figure 2.11) is simulated in PSCAD/EMTDC using both models. Circuit parameters—including the DC-link capacitor, inductor, and controller coefficients—are shown in the figure. The controller regulates the DC-link voltage by measuring and filtering it, comparing it with the 1.2 kV reference, and feeding the error into an integrator to generate the duty cycle for the gate pulses.

The DC side is represented by a controlled current-source that can supply positive or negative current. The DC current is initially set to zero until the voltage reaches steady state at 1.2 kV. It then steps to 0.2 kA at $t = 2$ s and to −0.2 kA at $t = 4$ s. The resulting waveforms for these current steps, illustrated in Figures 2.12 and 2.13, show that the AVM closely matches the detailed model while leaving out high-frequency switching effects.

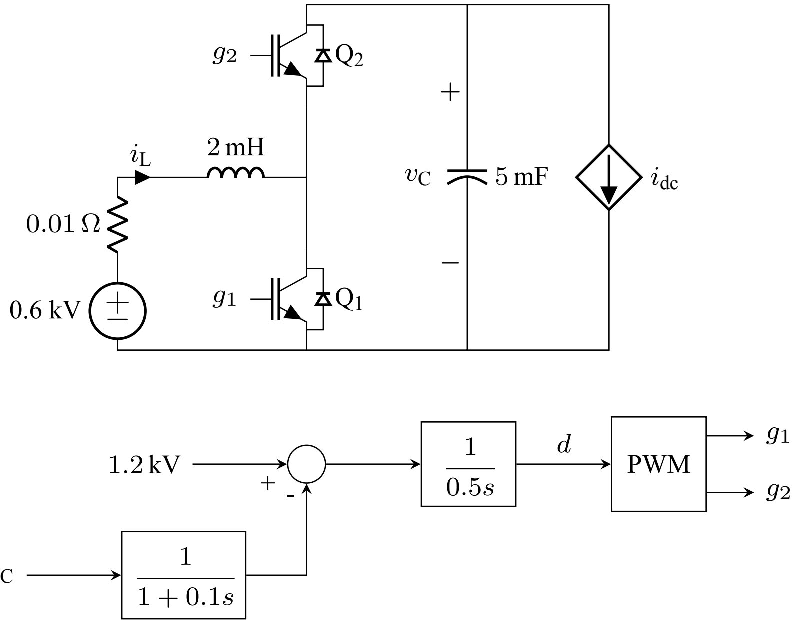

Figure 2.11: A controlled DC-DC converter used for model validation.

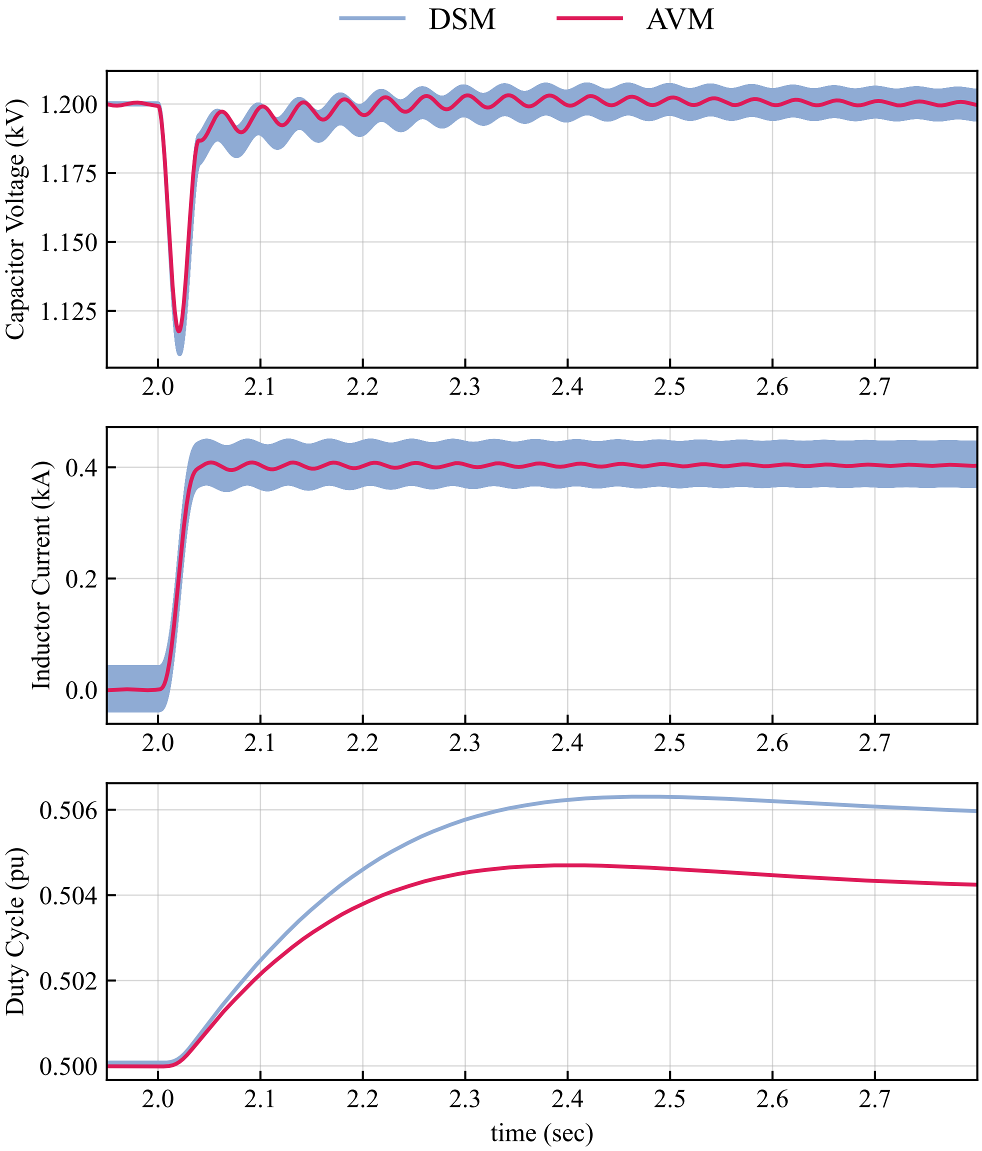

Figure 2.12: Comparison of the DC–DC converter AVM and detailed switching model responses to a step change of 0.2 kA in DC current.

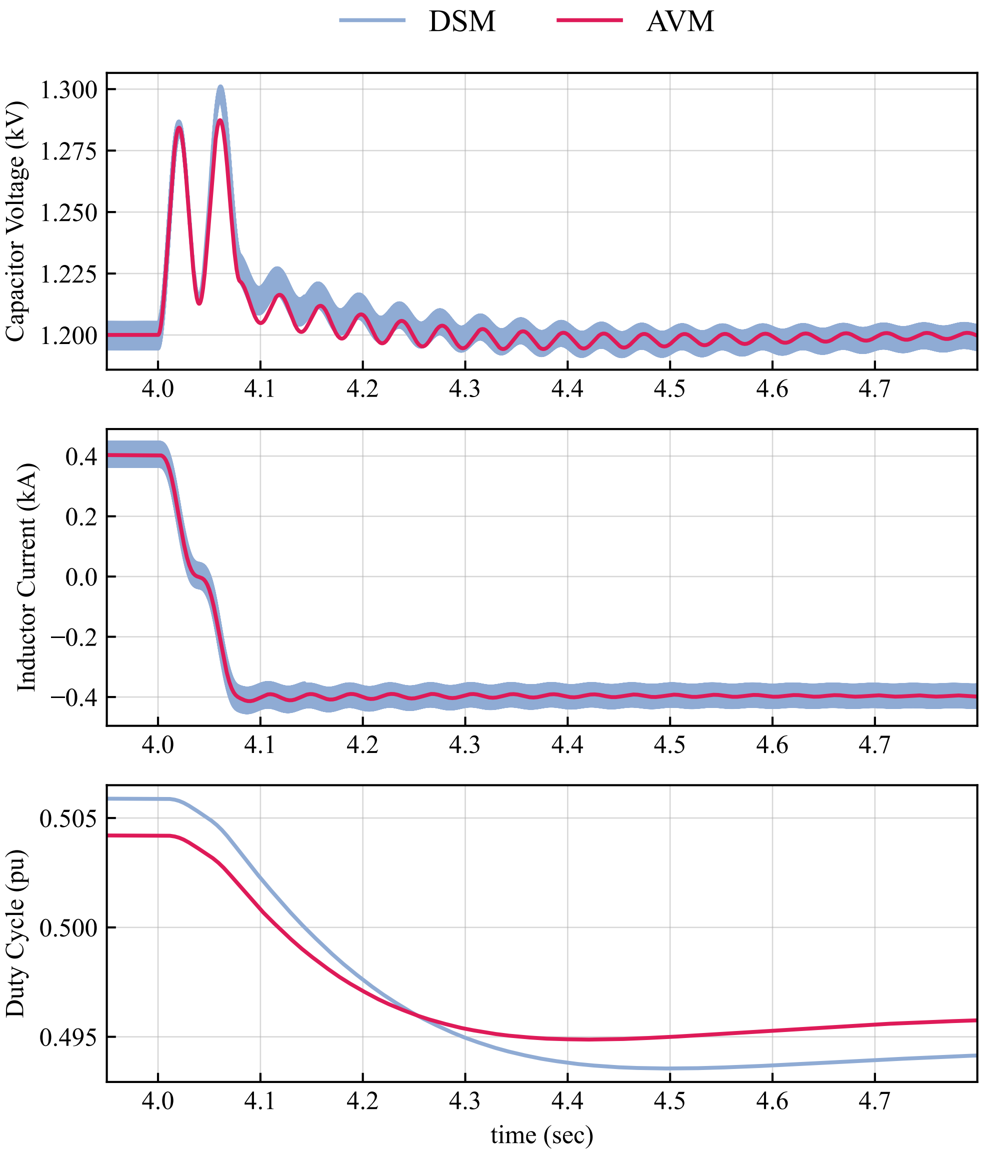

Figure 2.13: Comparison of the DC–DC converter AVM and detailed switching model responses to a step change to -0.2 kA in DC current.

2.7 Validation of the VSC Model

To validate the AVM of the VSC against a detailed switching model, the controlled VSC shown in Figure 2.14 is simulated in PSCAD/EMTDC. The DC-side voltage is assumed to be nearly constant, and the converter is connected to the AC system through a low-pass filter. The decoupled control strategy described earlier is employed to regulate the active and reactive power at the point of interconnection.

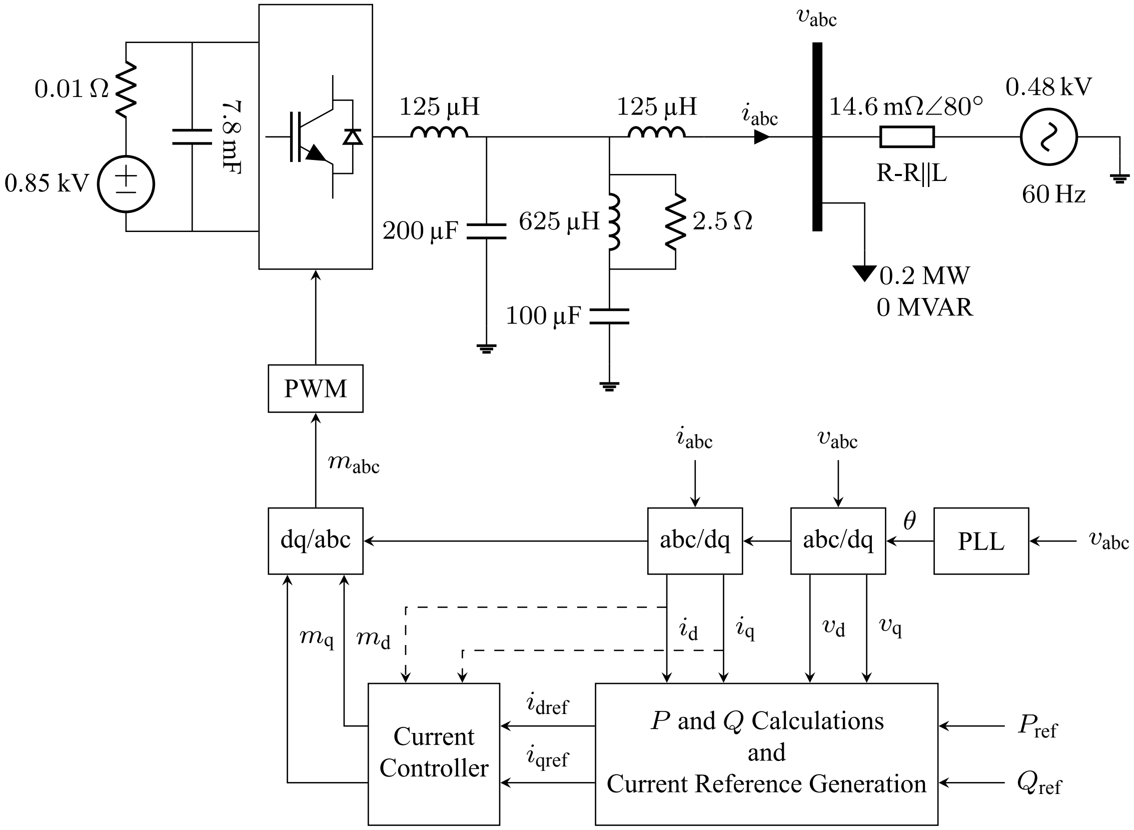

Figure 2.14: A controlled VSC for model validation.

The active power reference is stepped from 0.2 MW to 0.4 MW at $t = 2$ s, while the reactive power reference is kept at zero. At $t = 3$ s, the reactive power reference is stepped from 0 to

0.1 MVAR. The results presented in Figures 2.15 and 2.16 demonstrate that the AVM accurately reproduces the low-frequency contents of the response of the detailed switching model. The active power, reactive power, d- and q-axis currents, and d- and q-axis modulation waveforms obtained from the AVM closely match the low-frequency contents of the corresponding waveforms of the detailed switching model.

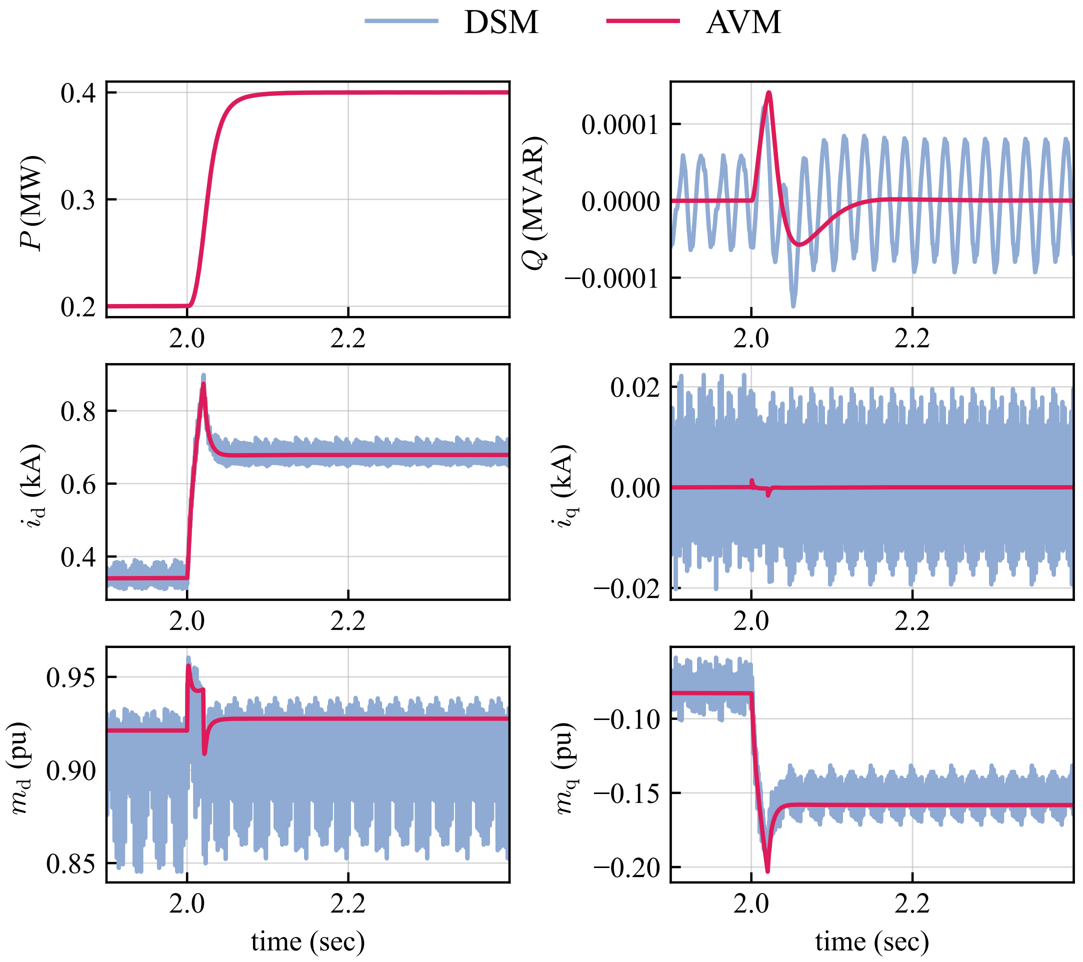

Figure 2.15: Comparison of the VSC's AVM and detailed switching model responses to a step change in active power.

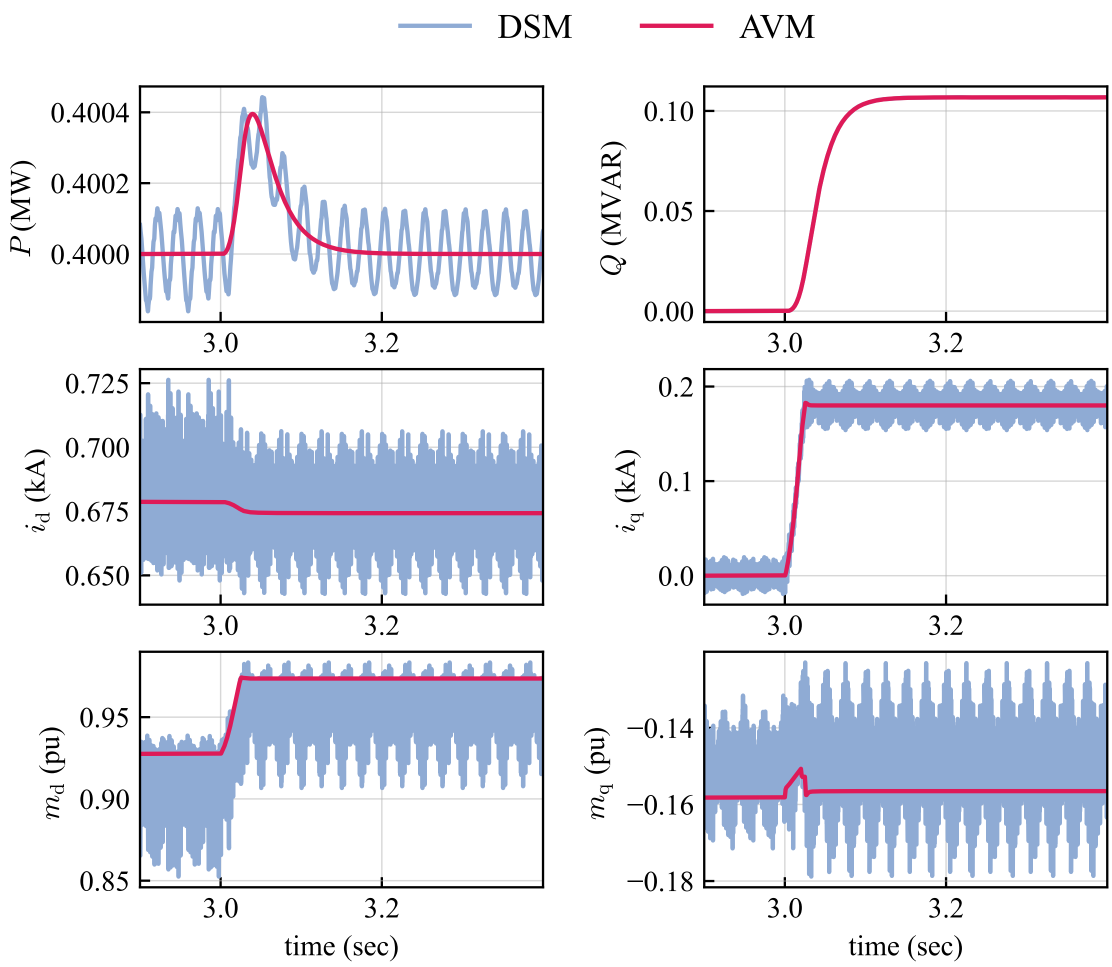

Figure 2.16: Comparison of the VSC's AVM and detailed switching model responses to a step change in reactive power.

It is worth noting that the steady-state operating point calculated using equations (2.29) and (2.30) yields $(m_\mathrm{d}, m_\mathrm{q}) = (0.92, -0.15)$ and $(m_\mathrm{d}, m_\mathrm{q}) = (0.96, -0.15)$ for the final active and reactive power reference sets in Figure 2.15 and Figure 2.16, respectively. These values are in close agreement with the AVM results, as observed in the waveforms of m_d and m_q in the same figures.

2.8 Conclusion

In this chapter, detailed modeling and control strategies for BESS were developed. The battery was represented using an equivalent circuit model incorporating the Shepherd equation. AVMs were derived for both the bidirectional DC-DC converter and the 2-level VSC using circuit averaging techniques, which eliminate high-frequency switching contents while preserving low-frequency behaviors essential for grid-level studies. This approach is aimed at reducing computational demands compared to detailed switching models, making it suitable for large-scale simulations involving multiple BESS units.

Control schemes were established for the DC-DC converter to regulate the DC-link voltage via duty cycle adjustment and for the VSC to independently manage active and reactive power using a decoupled control strategy. Model validations using PSCAD/EMTDC simulations confirmed that the AVMs closely replicate the responses of detailed switching models to step changes in current, active power, and reactive power. These validated models provide a robust foundation for studying BESS contributions to frequency regulation and system stability in subsequent chapters.

Chapter 3

A Framework for Automated Optimization in Power System Studies

3.1 Introduction

This chapter presents a practical framework for integrating electromagnetic transient (EMT) simulations (in PSCAD/EMTDC) with Python-driven optimization workflows. The primary objective is to establish an automated, iterative procedure that enables parameter adjustment, simulation execution, performance evaluation, and solution convergence using optimization algorithms—all without requiring manual intervention. The framework is particularly suited for power system design and control problems where transient behavior is critical, such as controller tuning, fault response optimization, and stability enhancement.

While the implementation details involve programming, this discussion focuses on the architecture, methodology, and theoretical foundations of the framework.

Although the framework is not novel in its individual components, its value lies in the systematic integration and automation of established EMT simulation and optimization techniques into a unified workflow.

3.2 Need for Electromagnetic Transient Simulation

Various approaches exist for modeling and simulating power system transients. Utilities commonly rely on transient stability (TS) tools, such as PSS$^{®}$E, to assess grid performance under a range of operating conditions and contingencies. TS solvers prioritize the slower electromechanical dynamics of large interconnected systems while neglecting the rapid electrical transients in the network. Modern power systems, however, are no longer dominated by synchronous generators; instead, they increasingly rely on IBRs, which introduce fast and nonlinear dynamics that span several timescales. If these behaviors are not modeled properly, their contribution to instability, resonant conditions, and other unforeseen issues may be overlooked. Under this circumstance, EMT simulations are utilized to capture the detailed interactions between power electronic devices and the grid, ensuring reliable operation and planning [30]. The fast-changing composition of modern power systems, marked by increasing presence of IBRs, their known reliability concerns, and the rising complexity of IBR controls and plant designs, requires the adoption of advanced EMT simulation environments to effectively identify and mitigate reliability risks [50]. This growing dependence on EMT arises from key technical necessities:

High-frequency dynamics: TS programs use millisecond-range time steps to model low-frequency electromechanical behavior, inherently neglecting fast transients. In contrast, EMT simulations operate at microsecond-range resolutions, capturing instantaneous values to accurately represent power electronic switching, harmonic distortions, and surge phenomena [51, 52].

Power electronics dominance: IBRs—including wind, solar, and battery systems—depend on fast-acting converters. Only EMT simulations can model their detailed control loops and switching behavior; TS simulators rely on oversimplified averaged representations that lack sufficient fidelity.

Increased transient complexity: Reduced system inertia in IBR-dominated grids leads to faster and more widespread disturbances. EMT's wide frequency bandwidth is essential for comprehensive stability evaluation in such environments.

3.3 Optimization-Enabled Electromagnetic Transient Simulation (OE-EMTS)

As power systems expand and technology advances, sophisticated devices—such as HVDC systems, energy storage systems (ESS), synchronous static compensators (STATCOMs), STATCOMs with energy storage devices (E-STATCOMs), and FACTS controllers—are being widely integrated. This integration greatly complicates the task of designing and tuning control parameters for each device. The challenge arises from two key factors. Firstly, developing a complete mathematical model of the entire system is nearly impossible due to its complexity and scale; even when such models are constructed, the resulting equations are highly intricate and difficult to interpret or analyze effectively. Secondly, different system components interact dynamically with one another, even though each operates with its own independent control system, leading to unpredictable, coupled behavior.

The OE-EMTS framework integrates iterative optimization algorithms with high-fidelity electromagnetic transient simulations to systematically design and tune complex power systems. Unlike traditional trial-and-error approaches, OE-EMTS automates the evaluation of a large number of candidate configurations by coupling an optimization engine with a robust EMT solver such as PSCAD/EMTDC. This synergy enables the exploration of multidimensional parameter spaces, including controller gains, filter time constants, and BESS sizing and placement, all while respecting physical constraints and performance objectives such as voltage stability, transient response, and frequency regulation.

At the core of OE-EMTS is a closed-loop workflow where each candidate solution triggers a complete EMT simulation run. Input variables to be optimized are programmatically injected into the simulation model, and the resulting time-domain waveforms—voltages, currents, active/reactive power flows, and frequency deviations—are post-processed to compute objective functions and constraints. Advanced optimization techniques such as GA or particle swarm optimization, guide the search toward solutions that minimize overshoot during faults, reduce settling time in frequency regulation, or optimize BESS placement.

In this thesis, PSCAD/EMTDC serves as the simulation engine in the proposed framework for two reasons: (i) it is well-suited for studying power systems containing BESS and solar systems, where fast-acting power electronic controllers are utilized; and (ii) it can interface with Python as an external automation tool. In the optimization process, each candidate solution is evaluated by running a full EMT simulation, wherein input variables (e.g., controller gains, time constants, or BESS locations) are applied to the model, and the resulting waveforms (voltages, currents, power flows, frequency deviation) are analyzed.

3.4 Python as an Automation Tool in Power System Studies

Python has become a widely adopted tool for automation in power system engineering, driven by its ease of use, rich library ecosystem, and strong compatibility with specialized simulation platforms.

As a high-level, interpreted language, Python supports rapid script development for automating repetitive operations, handling large-scale data, and communicating with external software. Within power system analysis, Python is particularly effective in complex workflows—such as parameter tuning, simulation execution, and results analysis—thereby reducing manual effort.

A key advantage of Python is its integration with leading commercial power system simulation tools, allowing engineers to leverage the strengths of these platforms while automating processes. For instance, PSS®E, a widely used tool for transmission planning and analysis, provides a Python application program interface (API) known as `psspy`. This interface enables programmatic control over power flow calculations, dynamic simulations, contingency analysis, and optimal power flow studies. Scripts can automate batch processing of scenarios, such as running multiple load flow cases or performing stability assessments, which is particularly beneficial for optimization tasks where numerous iterations are required.

Similarly, PSCAD/EMTDC offers an automation library developed in Python, available to users since version 4.6.1. This library allows users to programmatically launch simulations, modify model parameters, extract output data, and integrate with external optimization algorithms. In EMT studies, Python scripts can automate the injection of candidate parameters into the model, execute simulations, and evaluate performance metrics, forming the backbone of iterative optimization frameworks.

Beyond tool-specific integrations, Python's rich library ecosystem enhances its role in power system optimization. Libraries such as NumPy [53] and SciPy [54] provide numerical computing capabilities for handling matrices and solving optimization problems. Optimization-focused packages, such as SciPy's `optimize` module and PyGAD for modeling complex problems, can be combined with simulation tools to implement algorithms like GA or particle swarm optimization. In the developed OE-EMTS framework, Python acts as the connecting layer that integrates

PSCAD/EMTDC simulations with optimization algorithms. By automating the variable adjustment and evaluation cycle, Python both streamlines the process and enables scalability to handle increasingly complex power systems dominated by IBRs. This process is illustrated in Figure 3.1.

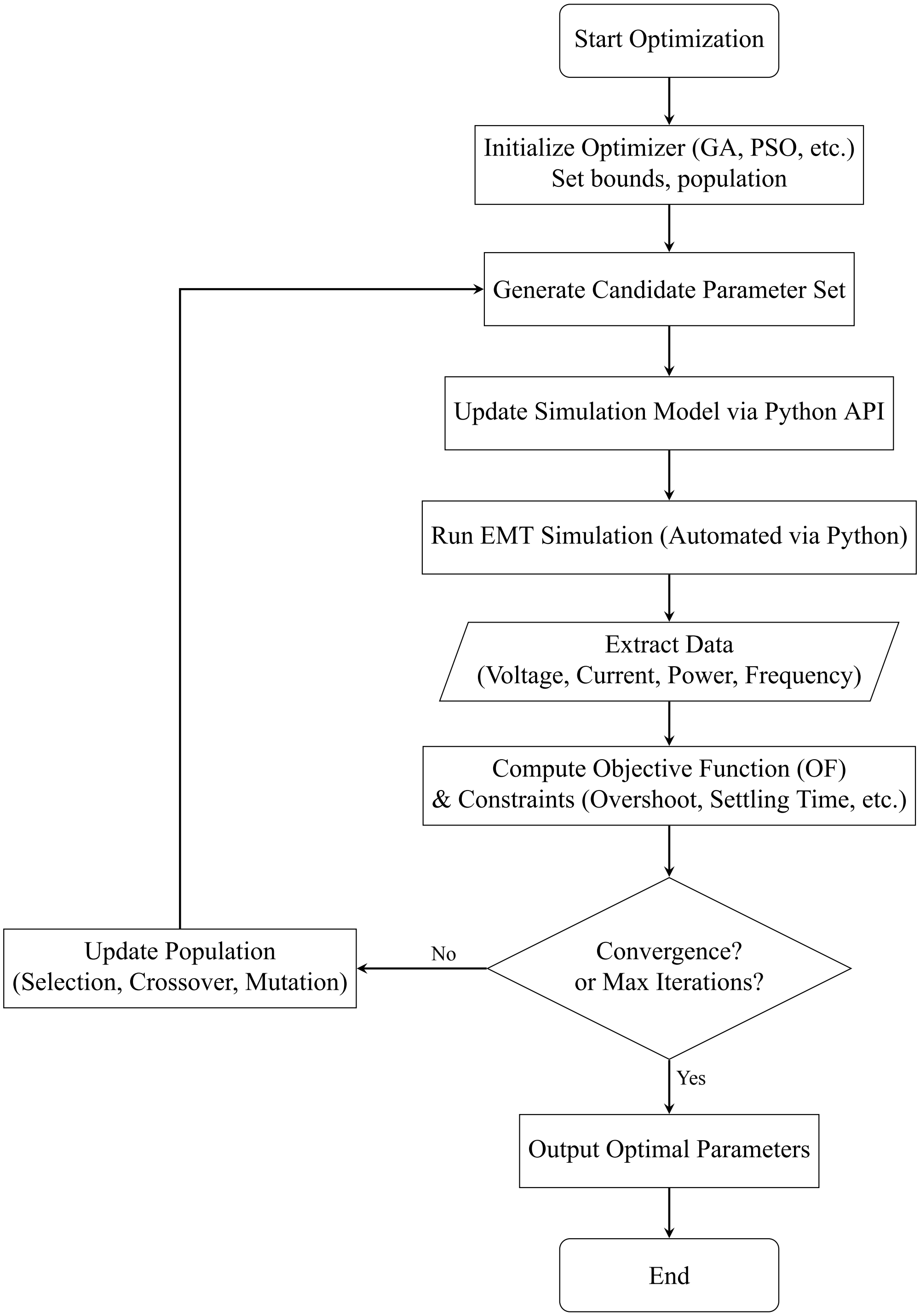

Figure 3.1: Flowchart of the OE-EMTS.

3.5 Optimization Algorithms for OE-EMTS

Optimization algorithms play a crucial role in the proposed OE-EMTS framework, as they guide the search for optimal parameter sets that enhance system performance. The OE-EMTS framework treats the EMT simulation as an evaluator of an OF. In power system applications, OFs are often nonlinear, non-convex, non-differentiable, and computationally expensive when they involve EMT simulations. Therefore, selecting a suitable optimization algorithm is essential to ensure robustness, efficiency, and reliability.

Optimization methods can broadly be categorized into deterministic and stochastic algorithms. Deterministic approaches, such as gradient descent and Newton–Raphson rely on derivative information and are generally effective for convex or smooth objective functions. However, their performance deteriorates when applied to complex, non-smooth or discontinuous problems—conditions frequently encountered in EMT-based studies due to switching events, control nonlinearities, and numerical noise [55]. Moreover, deterministic methods are prone to convergence toward local minima, making them less suitable for complex parameter landscapes.

In contrast, methods such as GA, PSO, and differential evolution employ probabilistic rules to explore the search space. These algorithms are derivative-free, flexible, and capable of avoiding local minima, which make them particularly attractive for optimization problems involving black-box simulations. In this thesis, GA is selected as the optimizer in OE-EMTS for the following technical and practical reasons.

1. **Alignment with the Computational Nature of EMT Simulations.** EMT simulations frequently exhibit abrupt changes in OF due to switching events, bus selection, loss of lines, etc. These effects, along with discrete (i.e., integer) decision variables such as bus location and number of BESS units, make the OF non-smooth and non-differentiable, thereby limiting the

suitability of gradient-based optimization methods. In contrast, the GA's population-based, derivative-free search is well suited to handling such non-smooth OF behavior.

2. **Natural Handling of Mixed Real and Integer Variables.** Power system design variables include continuous variables such as controllers gains and filter time-constants and discrete choices such as BESS bus location and tap settings. GA encodes both real- and integer-valued chromosomes.

3. **Proven Performance in the Literature of Power System Studies.** GA has been successfully applied to design of power system stabilizers [56], FACTS placement [57], real-time simulation of power systems [37], optimization of LCC-HVDC controller parameters [58], and optimizing parameters of a grid-forming modular multilevel converter [39].

4. **Implementation Simplicity via PyGAD.** The open-source Python library `PyGAD` [41] provides a high-level GA interface that integrates seamlessly with the PSCAD's automation library. Custom fitness functions, mutation rates, number of populations can be defined in fewer than 100 lines of code, enhancing ease of modification.

3.6 A Brief Formulation of GA

The GA is inspired by the process of natural evolution and operates on a population of N_p candidate solutions (also called chromosomes), each representing a possible combination of decision variables $\mathbf{x}_i = [x_{i1}, x_{i2}, \ldots, x_{in}]$, where n is the number of variables to be optimized. Each iteration (or generation) of the GA proceeds through the key steps briefly explained in following subsections. A comprehensive explanation of the GA is provided in [40].

3.6.1 Initialization

A population of N_p individuals is randomly generated within the defined bounds:

$$x_{ij} \in [x_j^{\text{min}}, x_j^{\text{max}}], \quad i = 1, 2, \ldots, N_\text{p};\ j = 1, 2, \ldots, n. \tag{3.1}$$

The initial population may be represented with the following matrix,

$$\mathbf{X}_\text{pop} = \begin{bmatrix} x_{11} & x_{12} & \cdots & x_{1N} \\ x_{21} & x_{22} & \cdots & x_{2N} \\ \vdots & \vdots & \ddots & \vdots \\ x_{N_\text{p}1} & x_{N_\text{p}2} & \cdots & x_{N_\text{p}N} \end{bmatrix}. \tag{3.2}$$

Typically, the elements of this $N_\text{p} \times N$ population matrix are initialized using a random number generator that produces normalized values in the range [0,1]. These values are then scaled to their corresponding limits as

$$x_{ij} = (x_j^{\text{max}} - x_j^{\text{min}}) y_{ij} + x_j^{\text{min}} \tag{3.3}$$

where y_{ij} denotes a uniformly distributed random variable between 0 and 1.

3.6.2 Fitness Evaluation

Each individual is evaluated by running a full EMT simulation in PSCAD/EMTDC. The performance is quantified by an objective (fitness) function $\text{OF}(\mathbf{x}_i)$, which may represent, for example, the weighted sum of transient overshoot, settling time, or voltage deviation:

$$\text{OF}(\mathbf{x}_i) = w_1 \cdot \text{OS}(\mathbf{x}_i) + w_2 \cdot \text{ST}(\mathbf{x}_i) + w_3 \cdot \text{VD}(\mathbf{x}_i), \tag{3.4}$$

where w_k are weighting coefficients assigned according to design priorities. Note that this process may involve reading output files resultant form the EMT simulations. This evaluation requires automated extraction of simulation outputs—typically from PSCAD-generated `.out` files—using Python scripts interfaced via PSCAD's automation library [42]. Signal processing (e.g., peak detection, settling time estimation) is performed with NumPy/SciPy to ensure robust and repeatable fitness computation.

3.6.3 Selection

The selection step in a GA is the process of choosing individuals from the current population to act as parents for the next generation, based on their fitness values. Individuals with higher fitness have a greater probability of being selected, which promotes the survival and reproduction of better solutions while still allowing weaker individuals a chance to maintain diversity.

3.6.4 Crossover (Recombination)

Pairs of selected parents exchange parts of their chromosomes to generate offspring. For continuous variables, a common approach is arithmetic crossover:

$$\mathbf{x}_{\text{child}} = \alpha\, \mathbf{x}_{\text{parent1}} + (1 - \alpha)\, \mathbf{x}_{\text{parent2}}, \tag{3.5}$$

where $\alpha \in [0, 1]$ is a random weighting factor.

3.6.5 Mutation

To maintain population diversity and avoid premature convergence, random perturbations are applied to selected genes as follows

$$x_{ij}^{\text{new}} = x_{ij} + \delta \tag{3.6}$$

where δ is a perturbation randomly chosen from a specified interval. If the new value exceeds the allowed bounds of that gene, it is adjusted according to the selected mutation handling strategy—such as clamping, wrap-around, or replacing it with a completely new random value.

3.6.6 Replacement and Termination

The offspring population replaces the current generation, and the process repeats until a termination criterion is met—typically when the best fitness value remains unchanged (or changes only negligibly) or when the maximum number of generations is reached. Figure 3.2 illustrates a flowchart of the GA.

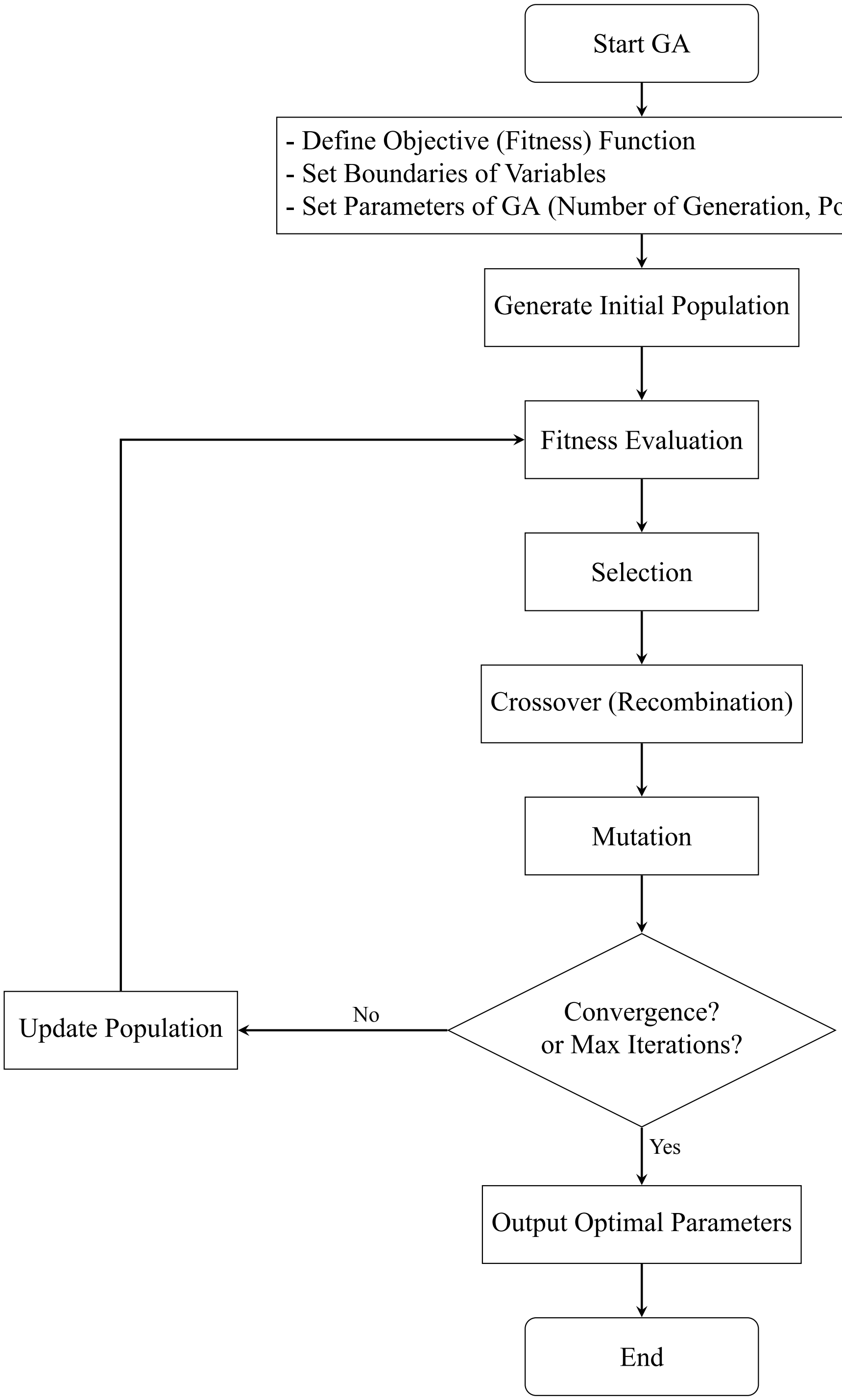

Figure 3.2: Flowchart of the GA.

3.7 Conclusion

This chapter outlined a comprehensive framework for OE-EMTS, integrating PSCAD/EMTDC simulations with Python-based automation to enable iterative parameter tuning without manual intervention. The necessity of EMT simulations was emphasized for capturing fast, nonlinear dynamics in modern inverter-dominated power systems, where traditional transient stability tools fall short. Python's role as an automation tool was highlighted, leveraging its libraries (e.g., NumPy, SciPy, PyGAD) and interfaces with simulation software to streamline workflows, including parameter injection, simulation execution, and objective function evaluation. Optimization algorithms were discussed, with GA selected for OE-EMTS due to its robustness in handling nonlinear, non-differentiable, and mixed real- and integer-valued variables, common in power systems. The GA formulation, including initialization, fitness evaluation, selection, crossover, mutation, and termination, was presented as an effective method for escaping local minima and exploring complex parameter spaces. This framework establishes the approach for power system design tasks such as controller tuning and BESS optimization.

Chapter 4

Case Study

In this chapter, optimal placement of a BESS is investigated in an exemplar 12-bus power system using OE-EMTS with the GA as the optimization engine. This 12-bus system incorporates both synchronous generation and a solar power plant. Candidate BESS locations are selected with the goal of optimization being to determine the most suited location as well as the size of the required BESS. The objective function considers both the frequency nadir, and a measure of the cost associated with the number of BESS units deployed.

4.1 Structure of the 12-Bus System

Figure 4.1 illustrates the 12-bus power system selected for demonstration in this study [59]. The system incorporates a solar PV power generation unit at Bus 11, while all other power generation units are conventional synchronous machines. The data for the transmission lines is summarized in Table 4.1. All synchronous machines share identical parameters listed in Table 4.2, except for their ratings, which are shown in Figure 4.1. The AC4A exciter model [60], shown in Figure 4.2, is employed for all machines, and its parameters are summarized in Table 4.3. The system was modeled and simulated in PSCAD/EMTDC, with the simulation running until all synchronous machines were fully initialized and the system reached steady state. Table 4.4 summarizes the rated bus voltages, loads, and compensation, along with the actual generation and bus voltages at steady state.

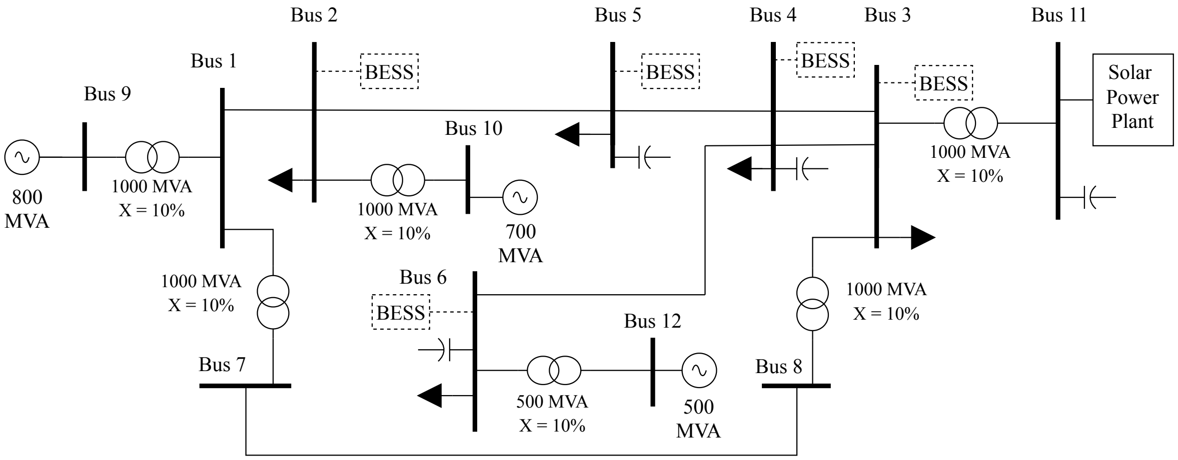

Figure 4.1: Schematic diagram of the 12-bus system [59].

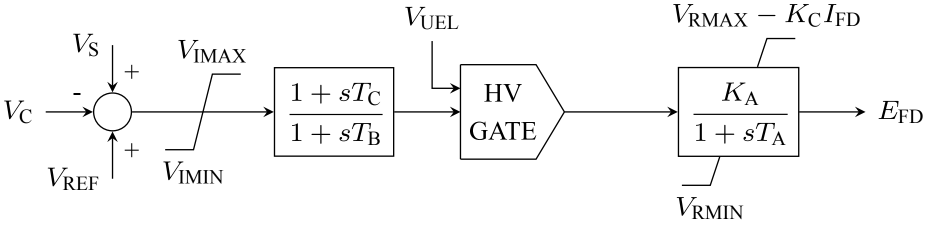

Figure 4.2: Schematic diagram of the AC4A exciter system.

Buses 2, 3, 4, 5, and 6, shown with dashed lines in Figure 4.1, are selected as candidate locations for the BESS. In practice, the placement of BESS units is not only a mathematical or optimization problem, but also subject to real-world constraints. For example, geographic and infrastructural limitations often restrict where BESS can actually be installed. In this case study, however, candidate buses are selected without accounting for these practical constraints, as the focus is solely on the optimization objective. These BESS units are connected to the system through closed breakers during initialization but remain idle, injecting no active or reactive power in steady state. A solution snapshot is then taken to avoid reinitializing the network and machines in subsequent simulations during the optimal BESS location search. After the snapshot, only one BESS remains connected in each simulation run, while the others are disconnected by opening their respective breakers.

Table 4.1: Transmission lines data.

Bus from	Bus to	Resistance [pu/km]	Reactance [pu/km]	Susceptance [pu/km]
1	2	1.144×10^{-4}	9.111×10^{-4}	1.82612×10^{-3}
1	6	3.356×10^{-4}	2.6653×10^{-3}	5.5477×10^{-3}
2	3	3.356×10^{-4}	2.6653×10^{-3}	5.5477×10^{-3}
3	4	1.144×10^{-4}	9.111×10^{-4}	1.82612×10^{-3}
4	5	1.144×10^{-4}	9.111×10^{-4}	1.82612×10^{-3}
5	6	3.356×10^{-4}	2.6653×10^{-3}	5.5477×10^{-3}
7	4	4.159×10^{-4}	1.7214×10^{-3}	3.2853×10^{-2}

Table 4.2: Synchronous machines data.

Parameter	Value	Unit
inertia constant, H	5	s
d-axis synchronous reactance, X_d	1.5	pu
q-axis synchronous reactance, X_q	1.2	pu
d-axis transient reactance, X'_d	0.4	pu
q-axis transient reactance, X'_q	0.228	pu
d-axis sub-transient reactance, X''_d	0.25	pu
q-axis sub-transient reactance, X''_q	0.25	pu
d-axis open-circuit transient time constant, T'_do	5.0	s
q-axis open-circuit transient time constant, T'_qo	0.85	s
d-axis open-circuit sub-transient time constant, T''_do	0.05	s
q-axis open-circuit sub-transient time constant, T''_qo	0.06	s

Table 4.3: Exciter parameters.

T_B [s]	T_C [s]	K_A [pu]	T_A [s]	V_Rmin [pu]	V_Rmax [pu]	K_C [pu]	V_Imin [pu]	V_Imax [pu]
0.0	0.0	20.0	0.05	-4.53	5.64	0.0	-10.0	10.0

Table 4.4: Load data.

Bus	Nominal Voltage [kV]	Load [MW+jMVAR]	Compensation [MVAR]	Generation [MW]	Voltage [pu]
1	230	-	-	-	1.041
2	230	280+j200	-	-	1.005
3	230	320+j240	-	-	0.982
4	230	320+j240	160	-	0.960
5	230	100+j60	80	-	0.988
6	230	440+j300	180	-	0.992
7	345	-	-	-	1.046
8	345	-	-	-	1.004
9	22	-	-	532	1.041
10	22	-	-	502	1.022
11	22	-	-	168	1.019
12	22	-	-	285	1.009

4.1.1 Solar Power Plant

The solar power generation unit, shown in Figure 4.3, is integrated into the AC system through a 2-level VSC, which facilitates precise control of active power and AC voltage at the point of interconnection (POI). Table 4.5 summaries the parameters of the converters and scaling component in the solar power plant system. To maintain a stable and regulated DC voltage at the VSC's DC terminal, a unidirectional boost converter is employed between the solar array and the VSC.

This boost converter ensures optimal voltage levels for efficient power transfer. To enhance the computational efficiency of the PSCAD/EMTDC simulation and reduce runtime, average-value models are utilized for both the VSC and the boost converter, simplifying the representation of their switching dynamics while preserving accuracy. The VSC employs a decoupled current controller within its inner loop control scheme, enabling independent regulation of active and reactive power components for robust grid integration. Meanwhile, the DC-DC boost converter operates using a maximum power point tracking (MPPT) algorithm to maximize energy harvest from the solar panels under varying environmental conditions. The MPPT tracker determines and outputs the reference voltage corresponding to the maximum available power point. This reference voltage is compared with the actual photovoltaic voltage, and the error is fed into a PI controller. The output of this PI controller serves as the reference power to be delivered by the DC-DC converter. This reference power is then compared with the actual DC output power, and the resulting error is processed by a second PI controller. The output of the second PI controller generates the appropriate duty cycle for the DC-DC converter to track the maximum power point effectively. The whole control process of this strategy is shown in Figure 4.4 along with the corresponding parameters listed in Table 4.6.

At the POI a scaling component is implemented to amplify the output current while maintaining the same voltage level, effectively representing the aggregated behaviour of a large-scale solar power plant. This approach models multiple solar panels and their associated converters connected to a common AC collector bus, significantly reducing the computational burden of EMT simulations while accurately capturing the of the entire solar power plant.

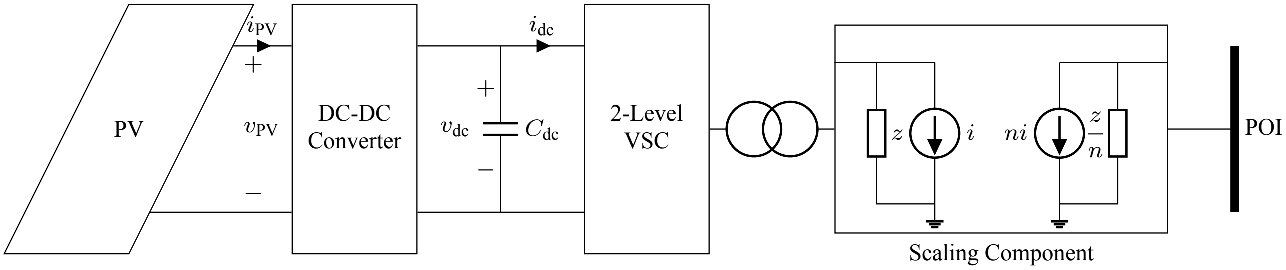

Figure 4.3: Schematic diagram of the solar power plant.

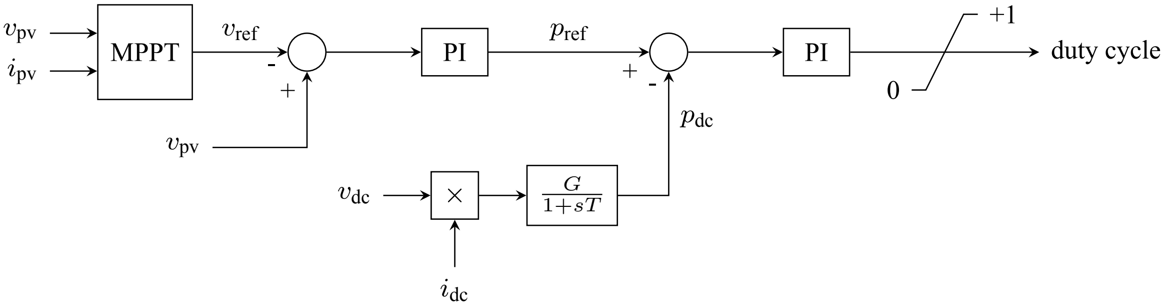

Figure 4.4: Control scheme of the DC-DC converter in the solar farm.

Table 4.5: Parameters of the converters in solar power plant.

Parameter	Value	Unit
DC-DC Converter		
Inductor	2.5	mH
DC link capacitor	10000	µF
Rated DC-link voltage	1.2	kV
Voltage Source Converter		
Series filtering inductor	0.9	mH
Parallel filtering capacitor	40	µF
Transformer		
Three-phase transformer MVA	0.25	MV A
Rated frequency	60	Hz
Converter-side rated voltage	0.65	kV
Grid-side rated voltage	22	kV
Leakage inductance	0.025	pu
Scaling Component		
Scale	668	-

Table 4.6: Parameters of the controller in Figure 4.4.

Parameter	Value	Unit
PI Controller Outputting Reference Power		
Proportional gain	0.01	pu
Time constant	0.1	s
PI Controller Outputting Duty Cycle		
Proportional gain	0.1	pu
Time constant	0.1	s
First-Order Filter		
Gain	1.0	pu
Time constant	0.01	s

4.1.2 Battery Energy Storage System

The BESS, illustrated in Figure 4.5, consists of a battery unit, a bidirectional DC-DC converter, and a 2-level VSC. Parameters of the BESS that do not vary across all generations of the GA are summarized in Table 4.7. A scaling component is employed at the POI to amplify the output current while preserving the voltage level, effectively modeling the collective behaviour of a large-scale BESS installation. The VSC regulates both active and reactive power delivered to the POI, while the DC-DC converter maintains a stable DC-bus voltage. For simplicity, the reactive power reference is set to zero, and the system design prioritizes optimal placement to enhance frequency response, which is closely tied to active power injection.

The control strategy for the BESS is derived from the swing equation, which describes the relationship between power system frequency dynamics, generation, and load. The swing equation is expressed as

$$2H\frac{\mathrm{d}f}{\mathrm{d}t} = P_{\text{gen}} - P_{\text{load}} = P_{\text{mech}} + P_{\text{solar}} + P_{\text{bat}} - P_{\text{load}} \tag{4.1}$$

where

f is the system frequency [pu],

H is the equivalent inertia constant of the power system [s],

P_{gen} is the total generated power [pu],

P_{load} is the total system load [pu],

P_{mech} is the mechanical power from synchronous generators [pu],

P_{solar} is the power output from solar PV systems [pu],

P_{bat} is the active power injected or absorbed by the BESS (positive for discharge, negative for charge) [pu].

The equivalent inertia constant H is the aggregate of the inertia constants of all synchronous machines, as given by

$$H = \sum_{i=1}^{n} H_i. \tag{4.2}$$

The system frequency, f, in the swing equation represents the frequency of the center of inertia (CoI) [61], defined as the weighted average of individual machine rotor frequencies (or speeds):

$$f = \frac{\sum_{i=1}^{n} H_i f_i}{\sum_{i=1}^{n} H_i} \tag{4.3}$$

where n is the number of synchronous machines, and f_i is the electrical frequency corresponding to the rotor speed of the i-th machine.

In practice, the CoI frequency is not directly measurable without access to all machine speeds [62]. Therefore, a local frequency measurement obtained via a PLL is commonly used [63, 64], though this introduces limitations in systems with low inertia.

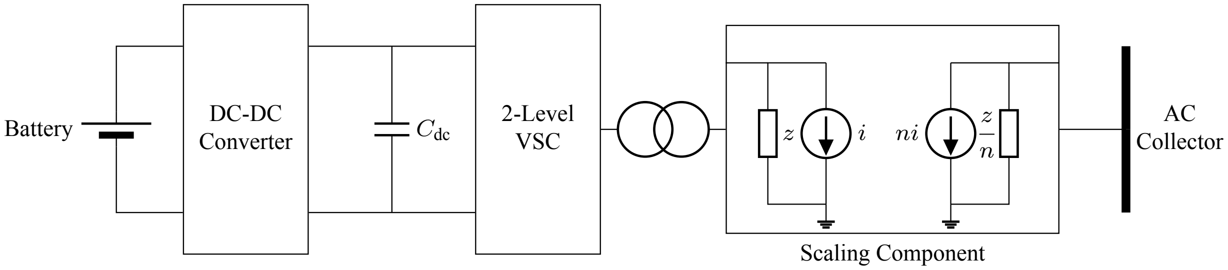

Figure 4.5: Schematic diagram of the BESS.

Table 4.7: Parameters of the converters used in BESS.

Parameter	Value	Unit
DC-DC Converter		
Inductor	1.0	mH
DC-link capacitor	25000	µF
Transformer		
Three-phase transformer MVA	3	MV A
Rated frequency	60	Hz
Converter-side rated voltage	0.723	kV
Grid-side rated voltage	230	kV
Leakage inductance	0.15	pu

The control architecture of the BESS, depicted in Figure 4.6, is tailored to improve the system's frequency response. System frequency is monitored at the POI using a PLL. To mitigate high-frequency oscillations arising from numerical inaccuracies in PLL frequency estimation, a first-order low-pass filter with a 50 ms time constant is applied to the measured frequency [65]. Additionally, a deadband block is incorporated after frequency deviation measurement to reduce the BESS control's sensitivity to minor, high-frequency disturbances. This deadband prevents unnecessary charge/discharge cycles, thereby prolonging the BESS lifespan [66]. The filtered frequency deviation is processed by a droop-based gain block with the droop of R_d, which generates a reference signal for the VSC to inject the necessary active power to counteract frequency deviations following a power system contingency. Under normal steady-state conditions, the BESS remains inactive, injecting no active or reactive power, and only engages when a frequency deviation is detected. The average of frequencies at all busses is calculated as the unique representative of the frequency of the whole system.

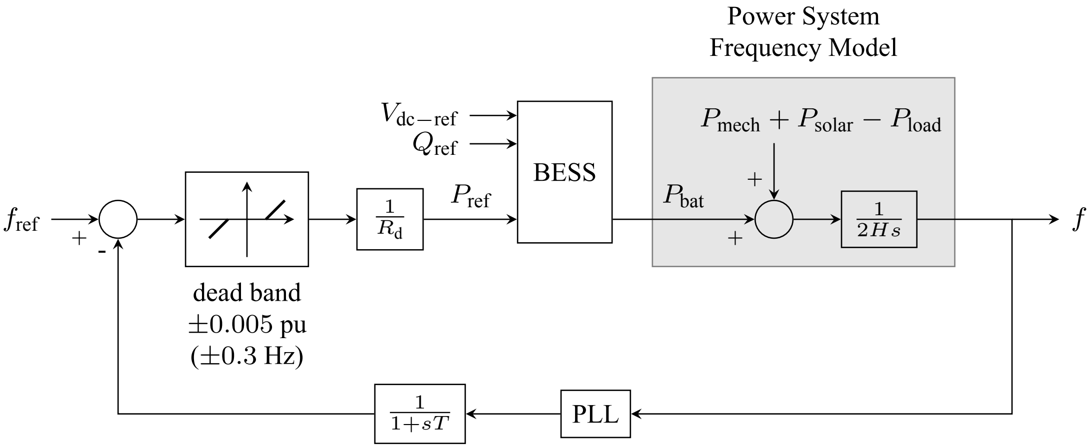

Figure 4.6: Control scheme of BESS for frequency regulation.

4.2 Simulation Results

In this study, a negative step change of 70% is applied to solar irradiation as a disturbance to mimic the appearance of cloudy weather conditions. As a result, the power injected by the solar system is suddenly reduced from 168 MW to 25 MW, leading to a drop in system frequency. The system frequency is defined as the average of the frequencies measured at each bus within the network. The objective function used in this study considers both the frequency deviation and the cost associated with the installed BESS, where the cost is assumed to be proportional to the number of BESS units. The objective function is expressed as

$$\mathrm{OF}(k, R_{\mathrm{d}}, n) = \Delta f_{\mathrm{nadir}} + W \times n, \tag{4.4}$$

where k is the bus location, R_{d} is the droop setting, n is the number of BESS units, $\Delta f_{\mathrm{nadir}}$ is the deviation of the frequency nadir from the nominal value (in per unit), and W is a weighting coefficient to balance the contributions of the two sub-objectives. The OF depends on three parameters: bus location, droop setting, and the number of BESS units in the scaling component. The droop setting is bounded between 1.25% and 10%, while the number of BESS units is restricted to between 10 and 90. The GA, using PSCAD/EMTDC as the function evaluator, is executed for the OF with various values of W, to generate several solutions to be assessed.

Table 4.8 summarizes the configuration of the PyGAD's GA. The algorithm evolves a population of 10 candidate solutions across 100 generations. Each solution contains 3 genes representing system parameters (bus location, droop, number of BESS units), with allowed values specified. A larger population size increases computational burden; for a problem with only three genes, a population of 10 is sufficient.

Table 4.8: GA configuration used in PyGAD.

Parameter	Value	Description
`num_generations`	100	Number of generations for the GA run.
`num_parents_mating`	4	Number of solutions selected as parents for mating.
`sol_per_pop`	10	Number of candidate solutions in each population.
`num_genes`	3	Number of variables in each solution (bus location, droop, number of BESS units).
`parent_selection_type`	`random`	Selection method for choosing parents.
`keep_parents`	2	Number of parents kept in the next generation without mating.
`crossover_type`	`single_point`	Method used to generate offspring from parents.
`mutation_type`	`random`	Mutation strategy used to alter gene values.
`mutation_percent_genes`	50%	Percentage of genes mutated in each solution.

The number of generations (100) was determined through trial and error, beyond which no significant improvement in results was observed. The number of parents selected for mating is typically between 30% and 50% of the population size; in this case, it is set to 4. Parent selection is performed randomly, and offspring are generated using single-point crossover.

Mutation is applied randomly to 50% of the genes in each solution. If the mutation rate is set too high (e.g., 80%), the algorithm behaves more randomly and may fail to converge. Conversely, if the mutation rate is too low, the algorithm may become trapped in local minima, limiting its ability to find the global optimum. In this study, a mutation rate of 50% is used, which effectively results in the mutation of approximately one gene out of the three in each solution.

It is evident that when $W = 0$, the GA selects the number of BESS units and droop gain values close to their boundary limits because increasing n and decreasing the droop gain consistently minimize the frequency deviation. The GA's results are reasonable, as it places the BESS near the two largest synchronous machines (see Figure 4.1) allowing for rapid power injection or absorption to damp out frequency excursions. Furthermore, the electrical distance between the BESS and the higher-rated synchronous machines is minimized, which helps reduce the effects of transmission line impedance and associated power losses.

However, by incorporating the cost term (dependent on n) into the OF, the optimization problem becomes more complex, leading to a more balanced solution. The PSCAD/EMTDC is run with a time-step of 50 microseconds for a simulation time horizon of 8 seconds. For each complete solution, running the GA over 100 generations takes approximately 42 hours to complete.

Figure 4.7 illustrates the simulation results corresponding to the parameters from the first row of Table 4.9. The figure shows that solar power is reduced by applying a negative step in irradiance, which leads to a frequency depression. To counteract this, the BESS injects real power based on the droop control mechanism. It is worth noting that the frequency deviation would be significantly higher without the installation of the BESS, as shown in the third subplot of the figure. Figure 4.8

further shows the frequency response when the same BESS (with identical number of units and droop setting) is installed at different locations. This demonstrates that the frequency nadir is dependent on the BESS location, emphasizing the importance of determining the optimal installation point.

Table 4.9: Optimal solution for different weighting parameters.

W	Bus Location	Number of BESS Units	Droop	Optimal Value of OF
0	2	90	1.39%	0.0096
0.00002	2	70	1.46%	0.0115
0.00005	2	35	1.25%	0.0127
0.0002	2	10	1.76%	0.0171
0.001	2	10	1.79%	0.0251

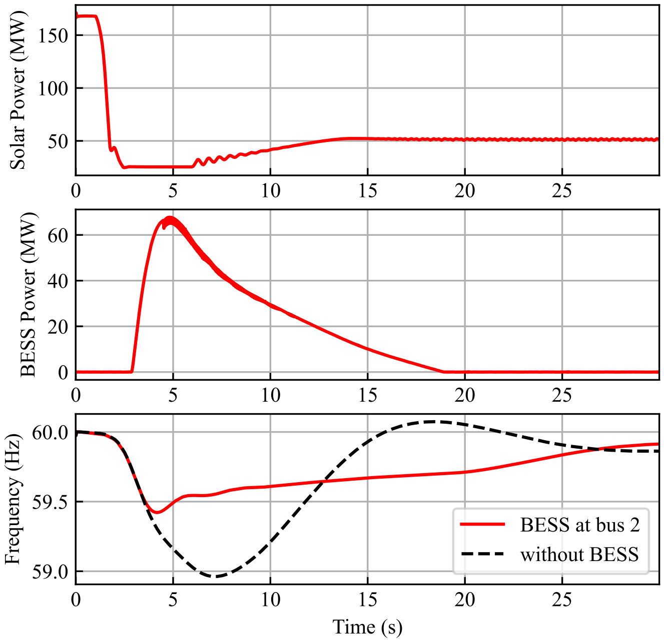

Figure 4.7: BESS response to solar power reduction.

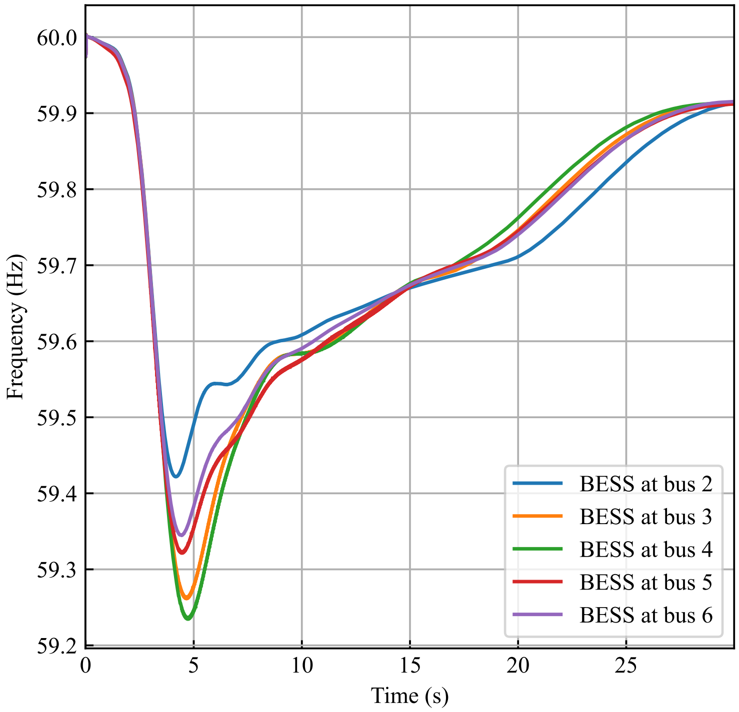

Figure 4.8: Frequency response for various BESS locations.

Figure 4.9 illustrates the OF values as the number of BESS units varies from 50 to 90 in increments of 10, with the BESS installed at bus 2 and the droop gain fixed at 1.46%, as specified in the second row of Table 4.9. As shown, the OF reaches its minimum when the number of BESS units is approximately 70, which aligns with the result produced by the GA. Additionally, Figure 4.10 shows the variation of the OF value with respect to the droop setting, assuming 70 BESS units are installed at bus 2. As expected, the OF value increases with higher droop settings, reaching its minimum at a droop value of 1.5%, which also aligns with the GA results.

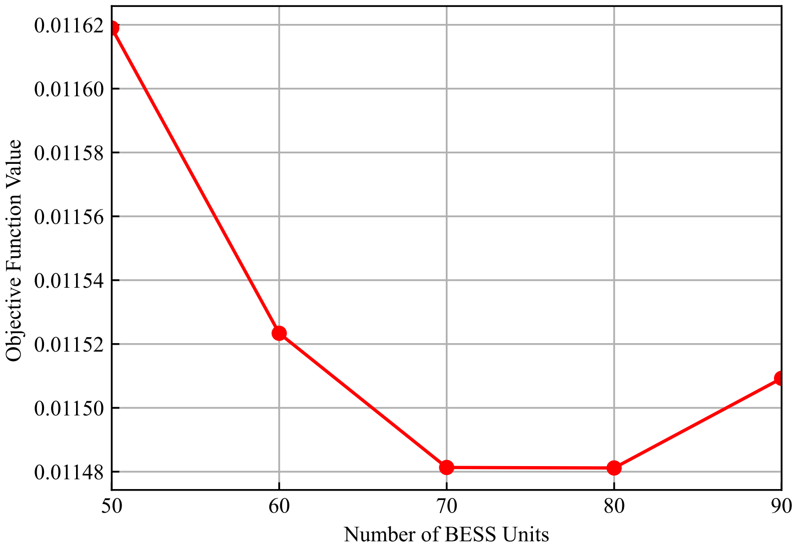

Figure 4.9: OF value vs. number of BESS units installed at bus 2 with the droop of 1.46%.

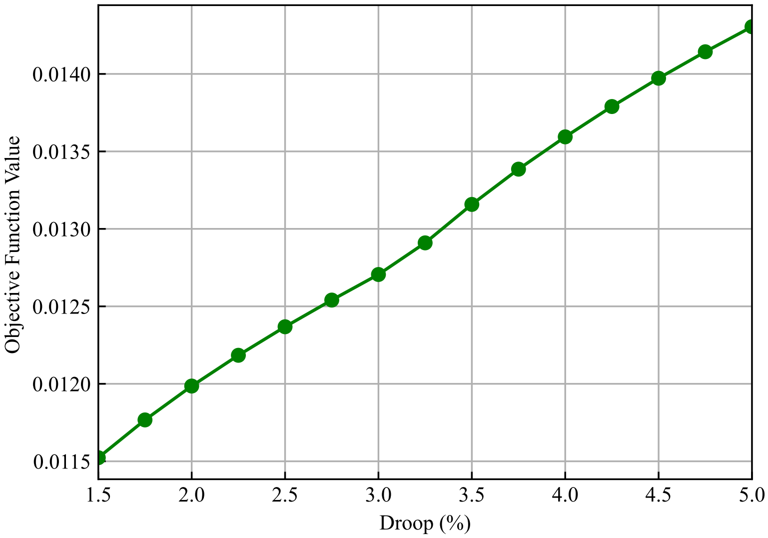

Figure 4.10: OF value vs. droop setting with 70 battery units installed at bus 2.

4.3 Conclusion

This chapter applied the proposed OE-EMTS framework to investigate the optimal placement and sizing of BESS in a 12-bus power system with significant renewable energy penetration. A GA was employed to identify the optimal BESS location, number of battery units, and droop control settings, with the objective function balancing frequency nadir improvement and BESS deployment cost.

Simulation results demonstrated that BESS location has a substantial impact on frequency response following disturbances, with certain buses providing significantly improved frequency nadir. The optimization results confirmed that strategic placement of BESS can achieve superior frequency regulation performance compared to arbitrary installation, even with a limited number of battery units. The case study validated the effectiveness of the proposed OE-EMTS framework in solving complex EMT-based optimization problems that involve both continuous and discrete decision variables.

Chapter 5

Contributions, Conclusions, and Recommendations for Future Work

5.1 Summary of Contributions

This thesis addressed the growing challenges of frequency regulation and dynamic stability in modern power systems with high penetration of IBRs. The primary objective was to develop an efficient and accurate framework for modeling, simulating, and optimizing the integration of BESS for frequency support, while overcoming the computational limitations of detailed EMT simulations.

The main contributions of this thesis can be summarized as follows.

Development of an AVM for BESS

An AVM of a complete BESS—comprising the battery, bidirectional DC–DC converter, and 2-level VSC—was developed using circuit-averaging techniques. The proposed model preserves the essential low-frequency dynamics required for grid interaction studies while eliminating high-frequency switching behavior. This aims to reduce computational burden without sacrificing modeling accuracy from the system perspective.

Formulation of OE-EMTS with GA

An OE-EMTS framework was introduced to integrate EMT simulations with external optimization algorithms. By utilizing Python as an automation layer, the framework enables fully automated parameter tuning, simulation execution, data extraction, and objective function evaluation, eliminating manual intervention and improving scalability and reproducibility. GA were employed as the optimization engine due to their robustness in handling non-linear, non-convex, and mixed-integer problems that are typically encountered in EMT-based studies. The thesis demonstrated that GA can effectively guide the optimization process when EMT simulations are used as objective function evaluators.

Application to Optimal BESS Placement for Frequency Regulation

The proposed framework was applied to a 12-bus power system with both synchronous generators and a solar power plant. The optimization process identified optimal BESS locations, sizing, and droop settings that improved frequency nadir performance while accounting for BESS deployment cost. The results highlighted the critical influence of BESS location and control parameters on system frequency response.

Publications

- M. Malekan, S. Filizadeh, ”Optimization of Battery Energy Storage System Placement and Parameters for Frequency Stability in Renewable-Intensive Power Systems,” in *Proc. CI-*

GRE International Symposium, Montreal, QC, Oct. 2025.

5.2 Conclusions

The results presented in this thesis lead to several important conclusions regarding the modeling, control, and optimization of BESS in modern power systems.

The developed AVM of the BESS provides an effective balance between accuracy and computational efficiency. It enables large-scale EMT simulations involving multiple candidate BESS locations without the excessive computational cost associated with detailed switching models.

Simulation results confirm that BESS, when properly controlled, can deliver rapid active power support and significantly improve frequency nadir following disturbances. This capability makes BESS a viable and flexible solution for mitigating the adverse effects of reduced system inertia caused by high renewable penetration.

The case study demonstrated that frequency response is highly sensitive to BESS placement, number of installed units, and droop settings. Optimal placement yields substantially better frequency regulation than arbitrary deployment, even with similar storage capacity.

The proposed OE-EMTS framework successfully combines the accuracy of EMT simulations with the flexibility of modern optimization algorithms. This approach provides a systematic alternative to traditional trial-and-error tuning and is particularly well-suited for converter-dominated power systems where fast dynamics are critical.

GA proved capable of navigating complex and discontinuous objective landscapes arising from EMT simulations. Its derivative-free and population-based nature makes it well-matched to optimization problems involving BESS placement and control.

5.3 Recommendations for Future Work

While this thesis provides a foundation for BESS optimization in EMT platforms, several areas remain for future research.

Integration of Grid-Forming Controls

This study focused on grid-following BESS controls. Future work should investigate the impact of grid-forming strategies, which could potentially provide even greater stability benefits in extremely low-inertia or islanded systems.

Consideration of Multiple Contingencies

The optimization could be expanded to consider a set of varied contingencies (e.g., three-phase faults, line trips, and different load shedding scenarios) to ensure the BESS placement is robust across all possible operational disturbances.

Real-Time Implementation

Although AVMs reduce computational effort, non-real-time EMT simulations are still computationally intensive. Therefore, implementing the OE-EMTS framework on real-time digital simulation platforms is recommended to achieve faster execution and improved overall simulation efficiency.

References

[1] M. J. B. Kabeyi and O. A. Olanrewaju, “Sustainable energy transition for renewable and low carbon grid electricity generation and supply,” *Frontiers in Energy Research*, vol. Volume 9 - 2021, 2022. [Online]. Available: https://www.frontiersin.org/journals/energy-research/articles/10.3389/fenrg.2021.743114

[2] International Renewable Energy Agency (IRENA), “Renewable power generation costs in 2023,” IRENA, Abu Dhabi, UAE, Tech. Rep., 2024. [Online]. Available: https://www.irena.org/Publications/2024/Sep/Renewable-Power-Generation-Costs-in-2023

[3] International Energy Agency (IEA), “Renewables 2023: Analysis and forecast to 2028,” IEA, Paris, France, Tech. Rep., 2023. [Online]. Available: https://www.iea.org/reports/renewables-2023

[4] C. Jin, N. Lu, S. Lu, Y. V. Makarov, and R. A. Dougal, “A coordinating algorithm for dispatching regulation services between slow and fast power regulating resources,” *IEEE Trans. Smart Grid*, vol. 5, no. 2, pp. 1043–1050, 2014.

[5] A. Keyhani and A. Chatterjee, “Automatic generation control structure for smart power grids,” *IEEE Trans. Smart Grid*, vol. 3, no. 3, pp. 1310–1316, 2012.

[6] R. Rajan, F. M. Fernandez, and Y. Yang, “Primary frequency control techniques for large-scale pv-integrated power systems: A review,” *Renewable and Sustainable Energy Reviews*, vol. 144, p. 110998, 2021. [Online]. Available: https://www.sciencedirect.com/science/article/pii/S1364032121002884

[7] NERC Inverter-Based Resource Performance Task Force (IRPTF), “Fast frequency response concepts and Bulk Power System reliability needs,” North American Electric Reliability Corporation, Tech. Rep., March 2020. [Online]. Available: https://www.nerc.com/globalassets/our-work/reports/white-papers/fast-frequency-response-concepts-and-bps-reliability-needs.pdf

[8] P. Kundur, *Power System Stability and Control*. New York: McGraw-Hill, 1994.

[9] ENTSO-E, “Rate of change of frequency (rocof) withstand capability,” 2018. [Online]. Available: https://eepublicdownloads.entsoe.eu/clean-documents/Network%20codes%20documents/NC%20RfG/IGD_RoCoF_withstand_capability_final.pdf

[10] ——, “Frequency stability evaluation criteria for the synchronous zone of continental europe,” 2016. [Online]. Available: https://www.entsoe.eu/Documents/SOC%20documents/RGCE_SPD_frequency_stability_criteria_v10.pdf

[11] H. T. Nguyen, G. Yang, A. H. Nielsen, and P. H. Jensen, “Frequency stability improvement of low inertia systems using synchronous condensers,” in *Proc. IEEE International Conference on Smart Grid Communications (SmartGridComm)*, Sydney, NSW, Australia, 2016, pp. 650–655.

[12] J. Fang, H. Li, Y. Tang, and F. Blaabjerg, “On the inertia of future more-electronics power systems,” *IEEE Journal of Emerging and Selected Topics in Power Electronics*, vol. 7, no. 4, pp. 2130–2146, 2019.

[13] H. Xu, Y. Wang, H. Liu, Y. Peng, Y. Liu, and L. Zengzhe, “A capacitor inertia based vsg and the stability analysis,” in *Proc. International Conference on Energy, Electrical and Power Engineering (CEEPE)*, Chongqing, China, 2021, pp. 38–43.

[14] S. M. Silmee and M. S. Hosen, “Virtual inertia enhancement using dc-link capacitors in wind integrated power plants,” in *Proc. International Seminar on Research of Information Technology and Intelligent Systems (ISRITI)*, Yogyakarta, Indonesia, 2021, pp. 480–486.

[15] K. Guo, Y. Tang, and J. Fang, “Exploration of the relationship between inertia enhancement and dc-link capacitance for grid-connected converters,” in *Proc. IEEE Southern Power Electronics Conference (SPEC)*, Singapore, 2018, pp. 1–7.

[16] G. Shahgholian and A. Fathollahi, “Advancing load frequency control in multi-resource energy systems through superconducting magnetic energy storage,” *AppliedMath*, vol. 5, no. 1, 2025. [Online]. Available: https://www.mdpi.com/2673-9909/5/1/1

[17] G. Magdy, A. Bakeer, and M. Alhasheem, “Superconducting energy storage technology-based synthetic inertia system control to enhance frequency dynamic performance in microgrids with high renewable penetration,” *Protection and Control of Modern Power Systems*, vol. 6, no. 4, pp. 1–13, 2021.

[18] Q. Long, A. Celna, K. Das, and P. Sørensen, “Fast frequency support from hybrid wind power plants using supercapacitors,” *Energies*, vol. 14, no. 12, 2021. [Online]. Available: https://www.mdpi.com/1996-1073/14/12/3495

[19] M. Krpan, I. Kuzle, A. Radovanović, and J. V. Milanović, “Modelling of supercapacitor banks for power system dynamics studies,” *IEEE Trans. Power Syst.*, vol. 36, no. 5, pp. 3987–3996, 2021.

[20] BloombergNEF. (2025, dec) Lithium-ion battery pack prices fall to $108 per kilowatt-hour, despite rising metal prices. [Online]. Available: https://about.bnef.com/insights/clean-transport/lithium-ion-battery-pack-prices-fall-to-108-per-kilowatt-hour-despite-rising-metal-prices-bloombergnef/

[21] S. A. Hosseini, M. Toulabi, A. Ashouri-Zadeh, and A. M. Ranjbar, “Battery energy storage systems and demand response applied to power system frequency control,” *International Journal of Electrical Power & Energy Systems*, vol. 136, p. 107680, 2022. [Online]. Available: https://www.sciencedirect.com/science/article/pii/S0142061521009108

[22] U. Akram, M. Nadarajah, R. Shah, and F. Milano, “A review on rapid responsive energy storage technologies for frequency regulation in modern power systems,” *Renewable and Sustainable Energy Reviews*, vol. 120, p. 109626, 2020. [Online]. Available: https://www.sciencedirect.com/science/article/pii/S1364032119308330

[23] L. Meng, J. Zafar, S. K. Khadem, A. Collinson, K. C. Murchie, F. Coffele, and G. M. Burt, “Fast frequency response from energy storage systems—a review of grid standards, projects and technical issues,” *IEEE Trans. Smart Grid*, vol. 11, no. 2, pp. 1566–1581, 2020.

[24] D. Zhu and Y.-J. A. Zhang, “Optimal coordinated control of multiple battery energy storage systems for primary frequency regulation,” *IEEE Trans. Power Syst.*, vol. 34, no. 1, pp. 555–565, 2019.

[25] S. Zhang, Y. Mishra, and G. Ledwich, “Battery energy storage systems to improve power system frequency response,” in *Proc. Australasian Universities Power Engineering Conference (AUPEC)*, Perth, WA, Australia, 2014, pp. 1–5.

[26] X. Luo, J. Wang, M. Dooner, and J. Clarke, “Overview of current development in electrical energy storage technologies and the application potential in power system operation,” *Applied Energy*, vol. 137, pp. 511–536, 2015. [Online]. Available: https://www.sciencedirect.com/science/article/pii/S0306261914010290

[27] K. Divya and J. Østergaard, “Battery energy storage technology for power systems—an overview,” *Electr. Power Syst. Res.*, vol. 79, no. 4, pp. 511–520, 2009.

[28] H. Chen, T. N. Cong, W. Yang, C. Tan, Y. Li, and Y. Ding, “Progress in electrical energy storage system: A critical review,” *Progress in Natural Science*, vol. 19, no. 3, pp. 291–312, 2009. [Online]. Available: https://www.sciencedirect.com/science/article/pii/S100200710800381X

[29] Energy Storage News, “Li-ion battery pack prices fell 8% since last year despite metals prices rising, bloombergnef says,” https://www.energy-storage.news/li-ion-battery-pack-prices-fell-8-since-last-year-despite-metals-prices-rising-bloombergnef-says/, dec 2025.

[30] B. Badrzadeh and R. Iravani, “The importance electromagnetic transient modeling and simulations: A key enabler for a successful energy transition [editor’s voice],” *IEEE Power and Energy Magazine*, vol. 23, no. 4, pp. 24–26, 2025.

[31] P. Krein, J. Bentsman, R. Bass, and B. Lesieutre, “On the use of averaging for the analysis of power electronic systems,” *IEEE Transactions on Power Electronics*, vol. 5, no. 2, pp. 182–190, 1990.

[32] S. EBRAHIMI, T. Vahabzadeh, and J. Jatskevich, “Numerically efficient average-value model for voltage-source converters in nodal-based programs,” *IEEE Open Journal of Power Electronics*, vol. 5, pp. 93–105, 2024.

[33] M. Rawa, A. Abusorrah, Y. Al-Turki, S. Mekhilef, M. H. Mostafa, Z. M. Ali, and S. H. E. A. Aleem, “Optimal allocation and economic analysis of battery energy storage systems: Self-consumption rate and hosting capacity enhancement for microgrids with high renewable penetration,” *Sustainability*, vol. 12, no. 23, 2020. [Online]. Available: https://www.mdpi.com/2071-1050/12/23/10144

[34] M. A. Abdulgalil, M. Ali, F. S. Al-Ismail, and M. Khalid, “One-step solution for sizing and allocation of battery energy storage system using dc optimal power flow,” in *Proc. International Conference on Renewable Energy Research and Application (ICRERA)*, Istanbul, Turkey, 2022, pp. 379–384.

[35] K. Khalid Mehmood, S. U. Khan, S.-J. Lee, Z. M. Haider, M. K. Rafique, and C.-H. Kim, “Optimal sizing and allocation of battery energy storage systems with wind and solar power dgs in a distribution network for voltage regulation considering the lifespan of batteries,” *IET Renewable Power Generation*, vol. 11, no. 10, pp. 1305–1315, 2017.

[36] Y. Zhang, Z. Y. Dong, F. Luo, Y. Zheng, K. Meng, and K. P. Wong, “Optimal allocation of battery energy storage systems in distribution networks with high wind power penetration,” *IET Renewable Power Generation*, vol. 10, no. 8, pp. 1105–1113, 2016.

[37] I. K. Park, “Real-time application of optimization-enabled electromagnetic transient simulation,” Ph.D. dissertation, University of Manitoba, Winnipeg, 2012.

[38] S. Filizadeh, A. M. Gole, D. A. Woodford, and G. D. Irwin, “An optimization-enabled electromagnetic transient simulation-based methodology for hvdc controller design,” *IEEE Trans. Power Del.*, vol. 22, no. 4, pp. 2559–2566, 2007.

[39] C. Jiang, J. S. Acosta, and A. M. Gole, “Optimizing the performance of a new current source type grid-forming modular multilevel converter using genetic algorithms,” *Electr. Power Syst. Res.*, vol. 234, p. 110808, 2024. [Online]. Available: https://www.sciencedirect.com/science/article/pii/S0378779624006941

[40] R. L. Haupt and S. E. Haupt, *Practical Genetic Algorithms*, 2nd ed. John Wiley & Sons, Ltd, 2004.

[41] A. F. Gad, “PyGAD: An intuitive genetic algorithm python library,” https://pygad.readthedocs.io, 2023, accessed: 2025-11-11.

[42] Manitoba Hydro International (MHI). Automation library. [Online]. Available: https://www.pscad.com/software/pscad/automation-library

[43] A. Ortega and F. Milano, “Generalized model of vsc-based energy storage systems for transient stability analysis,” *IEEE Trans. Power Syst.*, vol. 31, no. 5, pp. 3369–3380, 2016.

[44] M. Farrokhabadi, S. König, C. A. Cañizares, K. Bhattacharya, and T. Leibfried, “Battery energy storage system models for microgrid stability analysis and dynamic simulation,” *IEEE Trans. Power Syst.*, vol. 33, no. 2, pp. 2301–2312, 2018.

[45] O. Tremblay, L.-A. Dessaint, and A.-I. Dekkiche, “A generic battery model for the dynamic simulation of hybrid electric vehicles,” in *Proc. IEEE Vehicle Power and Propulsion Conference*, Arlington, TX, USA, 2007, pp. 284–289.

[46] R. W. Erickson and D. Maksimović, *Circuit Averaging, Averaged Switch Modeling, and Simulation*. Cham: Springer International Publishing, 2020, pp. 547–583.

[47] F.-B. Wu, B. Yang, and J.-L. Ye, *Chapter 4 - Operation control technology of energy storage systems*. Academic Press, 2019, pp. 83–151. [Online]. Available: https://www.sciencedirect.com/science/article/pii/B9780128152928000046

[48] A. Yazdani and R. Iravani, *Space Phasors and Two-Dimensional Frames*. Wiley-IEEE Press, 2010, pp. 69–114.

[49] ——, *Grid-Imposed Frequency VSC System: Control in dq-Frame*. Wiley-IEEE Press, 2010, pp. 204–244.

[50] North American Electric Reliability Corporation (NERC), “Reliability Guideline Recommended Practices for Performing EMT System Studies for Inverter-Based Resources,” Reliability Guideline, NERC, dec 2024, available: https://www.nerc.com/comm/RSTC_Reliability_Guidelines/Reliability_Guideline_Recommended_Practices_for_EMT_Studies_for_IBR_Approved.pdf.

[51] H. W. Dommel, “Digital computer solution of electromagnetic transients in single-and multiphase networks,” *IEEE Trans. on Power App. and Sys.*, vol. PAS-88, no. 4, pp. 388–399, 1969.

[52] H. Dommel and S. Bhattacharya, *EMTP Theory Book.* Microtran Power System Analysis Corporation, 1992.

[53] C. R. Harris, K. J. Millman, S. J. van der Walt, R. Gommers, P. Virtanen, D. Cournapeau, E. Wieser, J. Taylor, S. Berg, N. J. Smith, R. Kern, M. Picus, S. Hoyer, M. H. van Kerkwijk, M. Brett, A. Haldane, J. F. del Río, M. Wiebe, P. Peterson, P. Gérard-Marchant, K. Sheppard, T. Reddy, W. Weckesser, H. Abbasi, C. Gohlke, and T. E. Oliphant, “Array programming with NumPy,” *Nature*, vol. 585, no. 7825, pp. 357–362, Sep. 2020. [Online]. Available: https://doi.org/10.1038/s41586-020-2649-2

[54] P. Virtanen, R. Gommers, T. E. Oliphant, M. Haberland, T. Reddy, D. Cournapeau, E. Burovski, P. Peterson, W. Weckesser, J. Bright, S. J. van der Walt, M. Brett, J. Wilson, K. J. Millman, N. Mayorov, A. R. J. Nelson, E. Jones, R. Kern, E. Larson, C. J. Carey, İ. Polat, Y. Feng, E. W. Moore, J. VanderPlas, D. Laxalde, J. Perktold, R. Cimrman, I. Henriksen, E. A. Quintero, C. R. Harris, A. M. Archibald, A. H. Ribeiro, F. Pedregosa, P. van Mulbregt, and SciPy 1.0 Contributors, “SciPy 1.0: Fundamental Algorithms for Scientific Computing in Python,” *Nature Methods*, vol. 17, pp. 261–272, 2020.

[55] A. Gole, S. Filizadeh, R. Menzies, and P. Wilson, “Optimization-enabled electromagnetic transient simulation,” *IEEE Trans. Power Del.*, vol. 20, no. 1, pp. 512–518, 2005.

[56] Y. L. Abdel-Magid and M. A. Abido, “Optimal multiobjective design of robust power system stabilizers using genetic algorithms,” *IEEE Trans. Power Syst.*, vol. 18, no. 3, pp. 1125–1132, 2003.

[57] S. Gerbex, R. Cherkaoui, and A. J. Germond, “Optimal location of multi-type facts devices in a power system by means of genetic algorithms,” *IEEE Trans. Power Syst.*, vol. 16, no. 3, pp. 537–544, 2001.

[58] A. S. C. Leavy, L. Xu, S. Filizadeh, and A. M. Gole, “Simulation-based optimisation of lcc-hvdc controller parameters using surrogate model solvers,” in *Proc. Workshop on Control and Modeling for Power Electronics (COMPEL)*, Toronto, ON, Canada, 2019, pp. 1–8.

[59] S. Jiang, U. Annakkage, and A. Gole, “A platform for validation of facts models,” *IEEE Transactions on Power Delivery*, vol. 21, no. 1, pp. 484–491, 2006.

[60] “Ieee recommended practice for excitation system models for power system stability studies,” *IEEE Std 421.5-1992*, pp. 1–56, 1992.

[61] A. O. M. Federico Milano, *Power System Model*. John Wiley & Sons, Ltd, 2020, ch. 2, pp. 39–76. [Online]. Available: https://onlinelibrary.wiley.com/doi/abs/10.1002/9781119551881.ch2

[62] A. Ortega Manjavacas and F. Milano, "Chapter 6 - frequency definition and estimation in modern power systems," in *Converter-Based Dynamics and Control of Modern Power Systems*, A. Monti, F. Milano, E. Bompard, and X. Guillaud, Eds. Academic Press, 2021, pp. 125–147. [Online]. Available: https://www.sciencedirect.com/science/article/pii/B9780128184912000067

[63] F. Blaabjerg, R. Teodorescu, M. Liserre, and A. Timbus, "Overview of control and grid synchronization for distributed power generation systems," *IEEE Transactions on Industrial Electronics*, vol. 53, no. 5, pp. 1398–1409, 2006.

[64] A. Nicastri and A. Nagliero, "Comparison and evaluation of the pll techniques for the design of the grid-connected inverter systems," in *Proc. IEEE International Symposium on Industrial Electronics*, Bari, Italy, 2010, pp. 3865–3870.

[65] R. Parvari, S. Filizadeh, and I. Fernando, "Exploring the potential of grid-assisting MMCs with BESS in Manitoba's power infrastructure," in *Proc. CIGRE Canada Conference*, Winnipeg, Canada, 2024.

[66] A. Ortega Manjavacas, M. A. Adib Murad, J. Chen, M. Liu, T. O'Donnell, and F. Milano, "Chapter 7 - architectures for frequency control in modern power systems," in *Converter-Based Dynamics and Control of Modern Power Systems*, A. Monti, F. Milano, E. Bompard, and X. Guillaud, Eds. Academic Press, 2021, pp. 149–191. [Online]. Available: https://www.sciencedirect.com/science/article/pii/B9780128184912000079